

DUSTY CLOUD ACCELERATION BY RADIATION PRESSURE IN RAPIDLY STAR-FORMING GALAXIES

DONG ZHANG¹, SHANE W. DAVIS¹, YAN-FEI JIANG², AND JAMES M. STONE³

¹Department of Astronomy, University of Virginia, Charlottesville, VA 22904, USA

²Kavli Institute for Theoretical Physics, University of California, Santa Barbara, CA 93106, USA and

³Department of Astrophysical Sciences, Princeton University, Princeton, NJ 08544, USA

Draft version November 6, 2018

ABSTRACT

We perform two-dimensional and three-dimensional radiation hydrodynamic simulations to study cold clouds accelerated by radiation pressure on dust in the environment of rapidly star-forming galaxies dominated by infrared flux. We utilize the reduced speed of light approximation to solve the frequency-averaged, time-dependent radiative transfer equation. We find that radiation pressure is capable of accelerating the clouds to hundreds of kilometers per second while remaining dense and cold, consistent with observations. We compare these results to simulations where acceleration is provided by entrainment in a hot wind, where the momentum injection of the hot flow is comparable to the momentum in the radiation field. We find that the survival time of the cloud accelerated by the radiation field is significantly longer than that of a cloud entrained in a hot outflow. We show that the dynamics of the irradiated cloud depends on the initial optical depth, temperature of the cloud, and the intensity of the flux. Additionally, gas pressure from the background may limit cloud acceleration if the density ratio between the cloud and background is $\lesssim 10^2$. In general, a 10 pc-scale optically thin cloud forms a pancake structure elongated perpendicular to the direction of motion, while optically thick clouds form a filamentary structure elongated parallel to the direction of motion. The details of accelerated cloud morphology and geometry can also be affected by other factors, such as the cloud lengthscale, the reduced speed of light approximation, spatial resolution, initial cloud structure, and the dimensionality of the run, but these have relatively little affect on the cloud velocity or survival time.

Subject headings: galaxies: ISM — hydrodynamics — ISM: jets and outflows — methods: numerical — radiative transfer

1. INTRODUCTION

Galactic winds are ubiquitous in rapidly star-forming galaxies and starbursts. They are crucial to the formation and evolution of galaxies, shaping the galaxy luminosity function (Benson et al. 2003; Bower et al. 2012; Puchwein & Springel 2013), affecting the chemical evolution of galaxies (Erb 2008; Peebles & Shankar 2011; Barai et al. 2013; Makiya et al. 2014), determining the mass-metallicity relation (Tremonti et al. 2004; Finlator & Davé 2008), and regulating star and galaxy formation over cosmic time and polluting the intergalactic medium with metals (Aguirre et al. 2001a; Aguirre et al. 2001b; Oppenheimer et al. 2010). Many mechanisms have been proposed for driving galactic winds, including hot flow heated and driven by supernova explosions (Larson 1974; Dekel & Silk 1986; Chevalier & Clegg 1985; Strickland & Heckman 2009), radiation pressure by absorption in spectral lines or the continuum absorption and scattering of starlight on dust grains (Proga et al. 1998; Murray et al. 2005; Murray et al. 2010; Hopkins et al. 2012), cosmic rays (Ipavich 1975; Socrates et al. 2008; Uhlir et al. 2012), and photoevaporation heating by hot stars (Barkana & Loeb 1999; Shapiro et al. 2004; Iliiev et al. 2011).

Galactic winds have multi-phases over a broad range of temperature. Multiwavelength observations from radio to X-ray have been carried out to probe all types of gas and dust in winds (see Veilleux et al. 2005, and references therein). For example, soft and hard X-rays,

which are observed by the *Chandra X-ray observatory* and *XMM-Newton observatory*, have been used to constrain hot gas outflows (e.g., Strickland & Heckman 2007, 2009; Zhang et al. 2014; Chisholm et al. 2017). Also, emission lines such as H α , N II, O II, O III, and absorption lines such as Na I, K I, Mg II from near-IR and optical are observed to trace cold and warm gas in outflows, including molecular (e.g., Sakamoto et al. 1999; Veilleux et al. 2009; Cicone et al. 2014), neutral atomic (e.g., Heckman et al. 2000; Rupke et al. 2002, 2005a,b,c; Martin 2005; Kornei et al. 2013), and ionized gas (Shoppell & Bland-Hawthorn 1998; Martin 1998; Cooper et al. 2009).

The formation and acceleration of cold clouds in winds are still unknown. It is commonly believed that cold clouds are advected into winds. The prevailing picture is that these clouds are embedded in a hot wind, and driven out of the host galaxy by ram pressure of the hot wind (e.g., Murray et al. 2007; Strickland & Heckman 2009). However, clouds may be shredded and destroyed by hydrodynamic instabilities long before they reach the velocities required by observations (Klein et al. 1994; Poludnenko et al. 2002; Scannapieco & Brüggén 2015; Brüggén & Scannapieco 2016). It is uncertain whether cloud magnetization or fragmentation will significantly suppress the cloud disruption and push clouds to be co-moving with the hot wind (Cooper et al. 2009; McCourt et al. 2015, 2016). Recently, Thompson et al. (2016) suggested that although the initial cold clouds might be rapidly destroyed in the hot winds on small

scales, the hot flow may cool radiatively on larger scales, forming an extended region of cool gas (see also [Scannapieco 2017](#)). Then cold clouds can be self-induced by thermal instability and re-born again in the halo of host galaxy.

On the other hand, the radiation pressure of starlight on dust is also suggested as another mechanism to accelerate cold clouds in star-forming galaxies ([Murray et al. 2005](#); [Murray et al. 2011](#)). The evolution of dusty shells in the radiation-dominated regime has been well studied, both semi-analytically ([Thompson et al. 2015](#)), and numerically ([Krumholz & Thompson 2012, 2013](#); [Davis et al. 2014](#); [Tsang & Milosavljević 2015](#); [Rosdahl & Teyssier 2015](#); [Zhang & Davis 2017](#)). The dynamics of cloud acceleration by radiation pressure on dust is different from the dynamics of a dusty shell, because clouds only cover a small fraction of the solid angle from the host galaxy, and the cloud expansion behaves differently from a shell. It has been proposed that cold clouds may be ejected above the disk of the host galaxy by radiation from a single massive star cluster before any supernova explode, then radiation pressure from starlight in the disk may drive clouds to a distant of ~ 100 kpc ([Murray et al. 2005](#)). If the cloud is not pressure confined by its surrounding medium, it will expand at its internal sound speed, and reach very high velocities ([Murray et al. 2011](#); [Thompson et al. 2015](#)). However, all of the previous semi-analytic works are over-simplified in their assumptions or calculations. For example, the cloud is assumed to be a sphere, and turbulence and shredding are neglected in the cloud. The fully multi-dimensional radiation hydrodynamic simulations are needed to model the complicated properties and behaviors of the cloud during its acceleration and destruction.

A variety of algorithms for solving radiation hydrodynamics equations have been developed in the literature, including the traditional flux-limited diffusion method ([Levermore & Pomraning 1981](#); [Krumholz et al. 2007](#); [Turner & Stone 2001](#); [Zhang et al. 2011](#); [Krumholz & Thompson 2012, 2013](#)), the M1 closure method ([González et al. 2007](#); [Skinner & Ostriker 2013, 2015](#); [McKinney et al. 2014](#); [Rosdahl & Teyssier 2015](#)), the variable Eddington tensor (VET) method ([Stone et al. 1992](#); [Sekora & Stone 2010](#); [Davis et al. 2012](#); [Jiang et al. 2012](#)), and the Monte Carlo (MC) method ([Whitney 2011](#); [Tsang & Milosavljević 2015](#); [Roth & Kasen 2015](#); [Bisbas et al. 2015](#)). A comprehensive comparison of radiation hydrodynamic codes has not been carried out, but disagreements have been found for some specific problems. A code comparison similar to that carried out in [Bisbas et al. \(2015\)](#) for ionizing radiation would be benefited.

For the problem of the radiation-pressure-dominated flow and optically-thick dusty gas, [Krumholz & Thompson \(2012\)](#) studied the acceleration of dusty shells in a constant infrared radiation flux with a constant gravitational acceleration using the FLD method, and [Krumholz & Thompson \(2013\)](#) studied the interaction between a constant infrared flux and dusty gas but without gravity. They found that radiative Rayleigh-Taylor instability limits momentum transfer from radiation to gas to $\sim L/c$, where L is the radiation luminosity. [Rosdahl & Teyssier \(2015\)](#) found similar results using the M1 closure method. [Davis et al. \(2014\)](#) revisited the prob-

lems in [Krumholz & Thompson \(2012\)](#) using the VET method which directly solves the time-independent radiative transfer equation based on the short characteristic method, and found a stronger momentum coupling between radiation and gas compared to the results in [Krumholz & Thompson \(2012\)](#) in the systems with the initial infrared optical depth $\tau_{\text{IR}(\text{initial})} \sim 1 - 10$. Similar results were found in [Tsang & Milosavljević \(2015\)](#) who used the MC method. Moreover, in [Zhang & Davis \(2017\)](#) we revisited the problems in [Krumholz & Thompson \(2013\)](#) using the same VET method as in [Davis et al. \(2014\)](#) and also found more efficient momentum coupling between radiation and gas compared to the FLD results: the momentum transfer from radiation to gas is $\sim (1 + \epsilon)(L/c)$ with a boost factor $\epsilon \sim 1.6 - 23$ for $\tau_{\text{IR}(\text{initial})} \sim 1 - 10$. Since they directly solve the radiation transfer equation, the VET and MC methods are expected to give more accurate results than the FLD and M1 methods for dusty gas with low to moderate optical depth.

However, both the VET and the MC method have their own disadvantages. The intrinsic noise associated with Monte Carlo makes this method very expensive to simulate the dusty gas. The VET method uses the implicit differencing method which needs to invert large matrices every time step, therefore the VET method is also expensive. As an alternative to the VET method, an algorithm using explicit differencing of spatial operators to solve the time-dependent radiative transfer equation has been developed by [Jiang et al. \(2014\)](#). This radiation module was implemented in the MHD code ATHENA ([Stone et al. 2008](#)). Recently, a new radiation module ([Jiang et al. 2016, 2017](#)) which use a similar algorithm as in [Jiang et al. \(2014\)](#), has been implemented in a new MHD code ATHENA++, which is the upgraded version of ATHENA ([White et al. 2016](#); [Stone et al. 2017](#) in preparation). Radiation hydrodynamic simulations have explored the evolution of irradiated clouds in the active galactic nucleus (AGN) context ([Schartmann et al. 2011](#); [Proga et al. 2014](#); [Namekata et al. 2014](#); [Proga et al. 2015](#); [Waters & Proga 2016](#); [Waters et al. 2017](#)). In particular, [Proga et al. \(2014\)](#) investigated the effects of irradiation with various absorption and scattering opacities on the evolution of a cloud in the AGN environment, using the VET method with ATHENA. So far, no work has been done to simulate the cloud acceleration and evolution by radiation pressure on dust in a radiation-dominated regime. This paper is the first work to explore this question using the new radiation MHD ATHENA++ code.

This paper is organized as follows. In Section 2 we describe the radiation hydrodynamic equations, numerical methods, the reduced speed of light approximation, and the simulation setup. The parameters for our simulations are summarized in Table 1. We show the simulation results in Section 3, with different cloud characteristic lengthscales, background temperature, reduction factor for the speed of light, spatial resolution, and simulation dimensionality. In Section 4 we compare the cloud survival time in a radiation field to that in a hot flow, and discuss some secondary factors which may affect the cloud evolution. We also discuss the implications of the simulation results in Section 4. Conclusions are provided in Section 5.

2. METHODS AND INITIAL CONDITIONS

2.1. Equations

We solve the equations of mass, momentum, energy with radiation

$$\frac{\partial \rho}{\partial t} + \nabla \cdot (\rho \mathbf{v}) = 0, \quad (1)$$

$$\frac{\partial (\rho \mathbf{v})}{\partial t} + \nabla \cdot (\rho \mathbf{v} \mathbf{v} + \mathbf{P}) = -\mathbf{S}_r(\mathbf{P}), \quad (2)$$

$$\frac{\partial E}{\partial t} + \nabla \cdot (E \mathbf{v} + \mathbf{P} \cdot \mathbf{v}) = -c S_r(E). \quad (3)$$

Here ρ , \mathbf{v} , \mathbf{g} are the gas density, fluid velocity and the gravitational acceleration, $E = p/(\gamma-1) + \rho v^2/2$ is the total fluid energy density, with p being the gas pressure and $\gamma = 5/3$ being the gas adiabatic index. Also $\mathbf{S}_r(\mathbf{P})$ and $S_r(E)$ are the radiation source terms, which are discussed below. The time-dependent radiative transfer (hereafter RT) equation is

$$\frac{\partial I}{\partial t} + c \mathbf{n} \cdot \nabla I = S(I, \mathbf{n}). \quad (4)$$

The RT equation is similar as in Jiang et al. (2016). The basic algorithm for solving the RT equation was first described by Jiang et al. (2014), then modified by Jiang et al. (2016) (see also Jiang et al. 2017). The source terms $S(I, \mathbf{n})$, $\mathbf{S}_r(\mathbf{P})$ and $S_r(E)$ are no longer expanded to the first order of $\mathcal{O}(v/c)$ as in Jiang et al. (2014). Instead, the specific intensity $I(\mathbf{n})$ with angle \mathbf{n} in the lab frame is first transformed to the co-moving frame intensity $I_0(\mathbf{n}_0)$ via Lorentz transformation, where \mathbf{n}_0 is the angle in the co-moving frame. The source term S in the co-moving frame is

$$S(I_0, \mathbf{n}_0) = c \rho \kappa_{aR} \left(\frac{a_r T^4}{4\pi} - I_0 \right) + c \rho \kappa_s (J_0 - I_0) + c \rho (\kappa_{aP} - \kappa_{aR}) \left(\frac{a_r T^4}{4\pi} - J_0 \right), \quad (5)$$

where κ_{aR} and κ_{aP} are the Rosseland and Planck mean absorption opacities, κ_s is the scattering opacity respectively, and $J_0 = \int I_0(\mathbf{n}_0) d\Omega_0$ is the angular quadrature of the specific intensity in the co-moving frame. The radiation momentum and energy source terms $\mathbf{S}_r(\mathbf{P})$ and $S_r(E)$ in the co-moving frame are given by

$$\mathbf{S}_r(\mathbf{P}) = -\frac{\rho(\kappa_s + \kappa_{aR})}{c} \mathbf{F}_r, \quad (6)$$

and

$$S_r(E) = \rho \kappa_{aP} (a_r T^4 - E_r) \quad (7)$$

respectively, where \mathbf{F}_r is the radiation flux, and E_r is the radiation energy. $I_0(\mathbf{n}_0)$ is updated implicitly in the co-moving frame, and transformed back to the lab frame again via Lorentz transformation. The above radiation hydrodynamic equations are solved using the ATHENA++ radiation code.

For the infrared radiation in the rapidly star-forming regions with wavelength $\lambda \geq 10 \mu\text{m}$, the albedo of dust scattering is $\ll 1$ thus dust scattering is negligible compared to absorption (Draine 2003). We neglect dust scattering in the paper ($\kappa_s = 0$). For a Milky-Way-like dust-to-gas ratio, the infrared absorption opacity κ_{aR} and κ_{aP}

on dust can be calculated by (see Krumholz & Thompson 2012)

$$(\kappa_R, \kappa_P) = (10^{-3/2}, 10^{-1}) \left(\frac{T}{10 \text{ K}} \right)^2 \text{ cm}^2 \text{ g}^{-1}. \quad (8)$$

Equation (8) is valid for the dust temperature $T \lesssim 150 \text{ K}$, and κ_R becomes flat at the temperature range $150 \text{ K} \lesssim T \lesssim 1000 \text{ K}$, then the dust reaches its sublimation temperature at $T \simeq 1000 \text{ K}$ (Semenov et al. 2003). In this paper we assume that the gas temperature is the same as the dust temperature in the clouds $T_{\text{dust}} = T_{\text{gas}}$. We denote T_c as the cloud temperature and choose $T = T_c$ in equation (8). The justification of this assumption is discussed in Section 2.2.

2.2. Cloud Models

We define a constant infrared flux F_* and a characteristic temperature

$$T_* = \left(\frac{F_*}{a_r c} \right)^{1/4}, \quad (9)$$

Following the argument in Krumholz & Thompson (2013), the dust is considered to be initially in thermal equilibrium with the radiation field $T_{\text{dust}} = T_*$. The cloud is considered to be in “warm” starburst galaxies with a typical temperature $T_c \sim 10 - 100 \text{ K}$ (González et al. 2004; Thompson et al. 2005; Murray et al. 2007; Andrews & Thompson 2011; Scoville 2013; Vollmer et al. 2017). This is different from warm clouds in which photoheating balances radiative cooling and have $T_c \simeq 10^4 \text{ K}$. We assume that the cloud has an initial temperature of $T_c = T_* = 100 \text{ K}$ for both dust and gas in the cloud, and this gives the fiducial radiation flux $F_* = 5.6 \times 10^{13} L_\odot \text{ kpc}^{-2}$ with $T_{*,2} = T_*/100 \text{ K}$. This flux is comparable to some bright ultraluminous infrared galaxies (ULIRGs) with a star formation rate surface density $\Sigma_{\text{SFR}} \sim 9.7 \times 10^3 M_\odot \text{ yr}^{-1} \text{ kpc}^{-2}$ (Kennicutt 1998). In Section 4.5 we discuss other values of T_* and F_* based on observations. As the cloud evolves, the radiation energy density E_r in the cloud changes but the approximation $T_c \simeq T_r = (E_r/a_r c)^{1/4}$ holds. Davis et al. (2014) performed alternative simulations with $\kappa_{R,P} \propto T_r^2$ and compared to the standard simulations with $\kappa_{R,P} \propto T_c^2$ but found similar results.

Also, we define a characteristic acceleration

$$g_* = \frac{\kappa_{R,*} F_*}{c}, \quad (10)$$

which measures the radiation force on the dust. In this work we consider two groups of simulations with different characteristic lengthscales. One is defined as “large-scale” runs, in which the lengthscale is $h_* = 0.1 \text{ pc}$. Another group is defined as “small-scale” runs, which has a lengthscale of $h_* = c_{s,*}^2/g_*$, where $c_{s,*}$ is the characteristic sound speed. The small-scale h_* is the pressure scale height similar to the scales in Krumholz & Thompson (2012, 2013) (see also Davis et al. 2014; Zhang et al. 2017), and small-scale runs are important to address the turbulence behavior of the clouds. We perform different scale runs to study whether different lengthscales of the clouds change the cloud evolution. Moreover, we take

the cloud initial radius to be $r_* = 50h_*$, thus the large-scale cloud has a diameter of 10 pc, and the small-scale cloud has a diameter $\simeq 1 \times 10^{-3}$ pc for $T_* = 100$ K. Given different h_* , the characteristic timescale t_* for large-scale runs is

$$t_* = \frac{h_*}{c_{s,*}} \approx 1.1 \times 10^5 \text{ yr}, \quad (11)$$

while t_* for small-scale runs is

$$t_* = \frac{h_*}{c_{s,*}} \approx 1.2 \times 10^3 \text{ yr}. \quad (12)$$

Note that physically $t_* = 0.01t_{\text{cc}} = 0.01r_*/c_{s,*}$, where t_{cc} is the internal sound crossing time of the cloud.

The initial infrared optical depth of a cloud along its diameter is $\tau_* = 2\kappa_{\text{R},*}\rho_*r_*$, where ρ_* is the initial average density of the cloud. Observations show that the Na I carrying clouds have a typical column density $N_{\text{H}} \sim 10^{21} \text{ cm}^{-2}$ (e.g., Martin 2005; Wofford et al. 2013; Martin et al. 2015), which corresponds to $\tau_* \sim 0.01$. Another interesting consideration is the critical case $\tau_* = 1$, in which the infrared flux just becomes opaque to the cloud. The case $\tau_* = 1$ is still possible since it corresponds to a cloud column density $N_{\text{H}} \sim 2 \times 10^{23} \text{ cm}^{-2}$ or $\sim 1.5 \times 10^3 M_{\odot} \text{ pc}^{-2}$, which is lower than the gas surface density in typical luminous infrared galaxies (LIRGs) and ULIRGs. Thus, in this paper we consider $\tau_* = 0.01$ or 1 as the most interesting cases, but we also carry out simulations with $\tau_* = 3$ and 10 for comparison.

In our simulations the initial average density of the clouds is $\rho_* \sim 6.1 \times 10^3 \tau_* \text{ cm}^{-3}$ for large-scale runs, and $\rho_* \sim 5.4 \times 10^5 \tau_* \text{ cm}^{-3}$ for small-scale runs. Goldsmith (2001) studied that dust and gas can be thermally well coupled $T_{\text{dust}} = T_{\text{gas}}$ of $\rho_* \gtrsim 10^4 \text{ cm}^{-3}$. Thus the assumption that dust and gas in the cloud has a same temperature approximately holds for $\tau_* \gtrsim 1$ cloud, but the thermally coupling breaks down for $\tau_* = 0.01$. However, since the cloud is accelerated to be highly supersonic, the dynamics of the cloud is unlikely to be affected if we assume a different gas temperature from the dust temperature (Krumholz & Thompson 2013, Appendix A).

Similar to Davis et al. (2014), an initial density perturbation with $\delta\rho/\rho$ randomly distributed between -0.25 to 0.25 is put into the clouds. The perturbation is somewhat arbitrary, in Section 4.3 we discuss the effect of cloud initial turbulent structure on cloud dynamics and evolution.

2.3. Background Medium

If the cloud is not confined by the background pressure, it expands approximately at its sound speed. Thompson et al. (2015) showed that the semi-analytic model for cloud expansion and acceleration in a vacuum radiation field. However, it is more likely that the cloud is initially in approximate thermal pressure equilibrium with its surrounding medium (e.g., Spitzer 1968; Strickland & Heckman 2007; Scannapieco & Brügger 2015; Schneider & Robertson 2017). In general, a hot ionized ISM has a typical temperature $\sim 10^6$ K, and a warm ionized ISM has $\sim 10^4$ K. We assume that the cloud is embedded in the hot or warm ISM and in thermal pressure equilibrium with the ISM. We introduce the initial density ratio of the cloud to the background

medium $\chi_0 = \rho_*/\rho_{\text{bkgd}} = T_{\text{bkgd}}/T_*$, and consider two cases, $\chi_0 = 10^4$ and $\chi_0 = 10^2$, which corresponds to $T_{\text{bkgd}} = 10^6$ K and 10^4 K respectively. Here, we have dropped the dependence on the mean molecular weight and take $\mu = 1$. In Section 4.3 we consider the effect of molecular weights of the cloud and background. Also, we only include dust heating and cooling via radiation in our simulations, thus the background is adiabatic. We discuss the relevance of ionized background heating and cooling and the possibility that the cloud is not in pressure equilibrium with the background in Sections 4.2 and 4.4.

Thermal conduction can also be important due to temperature gradient between the cloud and background. There may be a large thermal conductive flux from the background to the cloud. In the case of saturated evaporation, Cowie & McKee (1977) showed that the cloud would be evaporated on a timescale (see also Faucher-Giguère et al. 2012)

$$t_{\text{evap}} \sim 1.5 \times 10^9 \text{ yr } N_{\text{H},23} T_{\text{c},2}^{-5/6} n_{\text{c},3}^{-1}, \quad (13)$$

where $N_{\text{H},23} = N_{\text{H}}/10^{23} \text{ cm}^{-2}$, $T_{\text{c},2} = T_{\text{c}}/100$ K and $n_{\text{c},3} = n_{\text{c}}/10^3 \text{ g cm}^{-3}$. Thus, we have

$$t_{\text{evap}} \sim 5.1 \times 10^8 \tau_*^{1/6} \text{ yr} \quad \text{for large-scale runs} \quad (14)$$

$$\sim 5.7 \times 10^6 \tau_*^{1/6} \text{ yr} \quad \text{for small-scale runs}, \quad (15)$$

both of which are much longer than t_* ($t_{\text{evap}} \gg t_*$). As a result, thermal conduction is not important based on the simply analytic estimate. Recent numerical simulations of clouds in hot galactic winds showed that thermal conduction may cause cold clouds to evaporate (e.g., Brügger & Scannapieco 2016; Waters & Proga 2016), but it has also been argued that conduction may be suppressed either by magnetic fields or plasma instabilities (McCourt et al. 2016). Nevertheless, in this work we neglect the effect of thermal conduction.

2.4. Reduced Speed of Light Approximation

If we use h_* as the unit for length, $c_{s,*}$ as the unit for velocity, $t_* = h_*/c_{s,*}$ as the unit for time, $a_r T_*^4$ as the unit for E_r and \mathbf{P}_r , and $ca_r T_*^4$ as the unit for \mathbf{F}_r , the RT equation (4) can be dimensionalized as

$$\frac{\partial \hat{I}}{\partial \hat{t}} + \mathbf{C}\mathbf{n} \cdot \nabla \hat{I} = \mathbb{C}\mathcal{S}(\hat{I}, \mathbf{n}), \quad (16)$$

where $\mathbb{C} = c/c_{s,*}$ is the ratio between the speed of light and the characteristic sound speed, and \hat{I} and \hat{t} are the dimensionless intensity and time. Since the fluid velocities are small compared to the speed of light to the order of $\mathcal{O}(v/c)$, one can reduce the speed of light and introduce a dimensionless parameter $\tilde{\mathbb{C}}$, where $\tilde{\mathbb{C}} \ll \mathbb{C}$ but $\tilde{\mathbb{C}} \gg 1$. The dimensionless RT equation (16) can be modified to

$$\frac{\partial \hat{I}}{\partial \hat{t}} + \tilde{\mathbb{C}}\mathbf{n} \cdot \nabla \hat{I} = \tilde{\mathbb{C}}\mathcal{S}(\hat{I}, \mathbf{n}). \quad (17)$$

We define the reduction factor $\mathbb{R} = \tilde{\mathbb{C}}/\mathbb{C}$ and take $\mathbb{R} = 10^{-2}$ as the fiducial value throughout the paper. We also test other reduction factors $\mathbb{R} = 10^{-1}$, $10^{-2.5}$ or 10^{-3} in Section 3.5.

Summary of Simulation Parameters

Run	dimensions	τ_*	h_*	χ_0	M_{hot}	$[L_x \times L_z]/h_*$	$N_x \times N_z$	$\Delta z/h_*$
T0.01L	2D	0.01	0.1 pc	10^4	–	400×1000	400×1000	1
T1L	2D	1	0.1 pc	10^4	–	400×1000	400×1000	1
T3L	2D	3	0.1 pc	10^4	–	400×1000	400×1000	1
T10L	2D	10	0.1 pc	10^4	–	400×1000	400×1000	1
T0.01S	2D	0.01	$c_{s,*}^2/g_*$	10^4	–	400×1000	400×1000	1
T1S	2D	1	$c_{s,*}^2/g_*$	10^4	–	400×1000	400×1000	1
T10S	2D	10	$c_{s,*}^2/g_*$	10^4	–	400×1000	400×1000	1
T0.01L_W	2D	1	0.1 pc	10^2	–	400×1000	400×1000	1
T1L_W	2D	1	0.1 pc	10^2	–	400×1000	400×1000	1
T1LR1	2D	1	0.1 pc	10^4	–	400×1000	400×1000	1
T1LR2.5	2D	1	0.1 pc	10^4	–	400×1000	400×1000	1
T1LR3	2D	1	0.1 pc	10^4	–	400×1000	400×1000	1
T1L_HR1	2D	1	0.1 pc	10^4	–	400×1000	800×2000	0.5
T1L_HR2	2D	1	0.1 pc	10^4	–	400×1000	800×4000	0.25 ^a
T1L_LR1	2D	1	0.1 pc	10^4	–	400×1000	200×500	2
T1L_LR2	2D	1	0.1 pc	10^4	–	400×1000	100×250	4
T0.01L_HR	2D	0.01	0.1 pc	10^4	–	400×1000	200×500	2
T0.01L_LR1	2D	0.01	0.1 pc	10^4	–	400×1000	200×500	2
T1L_3D1	3D	1	0.1 pc	10^4	–	$400^2 \times 1000$	$200^2 \times 500$	2
T1L_3D2	3D	1	0.1 pc	10^4	–	$400^2 \times 1000$	$100^2 \times 250$	4
H1	2D	–	2.8e-4 pc	10^4	5	400×1000	400×1000	1
H2	2D	–	1.1e-3 pc	10^4	10	400×1000	400×1000	1
H3	2D	–	4.5e-3 pc ^b	10^4	20	400×1000	400×1000	1

TABLE 1

NOTES: PARAMETER DEFINITIONS: τ_* IS THE INITIAL INFRARED OPTICAL DEPTH OF THE CLOUDS, h_* IS THE CHARACTERISTIC LENGTHSCALE, χ_0 IS THE INITIAL DENSITY RATIO OF THE CLOUDS TO THE BACKGROUND MEDIUM, M_{hot} IS THE MACH NUMBER IN HOT FLOWS GIVEN BY $V_{\text{hot}}/c_{s,\text{hot}}$, L_x AND L_z ARE THE LENGTH OF THE COMPUTATIONAL BOX ALONG x AND z DIRECTIONS IN UNIT OF h_* , AND N_x AND N_z ARE THE GRID ZONES ALONG x AND z DIRECTIONS. ^aFOR T1L_HR2 RUN $\Delta z/h_* = 0.25$ BUT $\Delta x/h_* = 0.5$. ^bFOR H1, H2 AND H3 RUNS THE LENGTHSCALE IS GIVEN BY $\tau_* h_*/(2\kappa_{R,*} \rho_*)$ WHERE $\rho_* = \chi_0 \rho_{\text{hot}}$, $h_* = 0.1$ PC, $\chi_0 = 10^4$ AND ρ_{hot} IS GIVEN BY EQUATION (22).

On the other hand, the dimensionless hydrodynamic momentum and energy equations can be written as

$$\frac{\partial(\hat{\rho}\hat{\mathbf{v}})}{\partial\hat{t}} + \nabla \cdot (\hat{\rho}\hat{\mathbf{v}}\hat{\mathbf{v}} + \hat{\mathbb{P}}) = \hat{\rho}\hat{\mathbf{g}} - \mathbb{P}\mathbf{S}_r(\mathbf{P}), \quad (18)$$

$$\frac{\partial\hat{E}}{\partial\hat{t}} + \nabla \cdot (\hat{E}\hat{\mathbf{v}} + \hat{\mathbb{P}} \cdot \hat{\mathbf{v}}) = \hat{\rho}\hat{\mathbf{g}} \cdot \hat{\mathbf{v}} - \mathbb{P}CS_r(E). \quad (19)$$

Comparing to equations (2) and (3), the quantities denoted with hat ($\hat{\cdot}$) are dimensionalized, and the parameter \mathbb{P} is defined as $\mathbb{P} = a_r T_*^4 / (\rho_* c_{s,*}^2)$ (Jiang et al. 2012). We solve dimensionless equations instead of equations (1), (2), (3) and (4), and hereafter skip the hat denotations for all the quantities. Note that \mathbb{C} in hydrodynamic equation (19) is not reduced. Importantly, the reduced speed of light only appears in the RT equation (see Gnedin (2016) for a detailed discussion). More details of the reduced speed of light approximation is discussed in Section 3.5 and Appendix A.

2.5. Initial Setup

We perform a series of 2D and 3D simulations on a Cartesian grid. In 2D runs x -coordinate is the horizontal direction, and z -coordinate is the vertical direction. In 3D runs we add y -coordinate as another horizontal direction. Flux F_* is injected at the bottom of the vertical direction as the radiation boundary. Other radiation boundary and all the hydrodynamic boundaries are set up as outflows. In all simulations, the computational box covers $(-200 h_*, 200 h_*)$ in x direction and $(-500 h_*, 500 h_*)$ in z direction, for 3D runs the box also covers $(-200 h_*, 200 h_*)$ in y direction. The cloud is located at

the center of the computational domain $(x, z) = (0, 0)$.

The mass-weighted cloud mean velocity during the cloud acceleration is given by

$$V_{\text{mean}} = \langle v_z \rangle = \frac{1}{M_c} \int_{V_c} \rho v_z dV. \quad (20)$$

The “flying distance” of the irradiated cloud along the vertical direction can be defined at the mass center of the cloud

$$z_c = \int_0^t V_{\text{mean}} dt. \quad (21)$$

Since z_c is much larger than the size of the box in most simulations, we adopt the cloud-following scheme to keep the cloud always at the center of the box. In cloud-following frame the cloud mean velocity along the vertical direction is always zero, and the background medium has a velocity of $-V_{\text{mean}}$. The vertical coordinate z is replaced by $z + z_c$ instead, but we still denote it as z .

Table 1 summarizes simulation parameters for our 2D and 3D radiation hydrodynamic runs with large-scale and small-scale of h_* and a range of cloud initial optical depth τ_* , reduction factor \mathbb{R} , density ratio χ_0 and resolutions. T0.01L, T1L, T3L and T10L denotes large-scale (L) runs with $\tau_* = 0.01, 1, 3$ and 10 respectively. T0.01S, T1S, T10S are small-scale (S) runs with $\tau_* = 0.01, 1$ and 10 . T0.01L_W and T1L_W are runs with $\chi_0 = 10^2$ so they fall to the case of warm (W) background with $T_{\text{bkgd}} = 10^4$ K. Since we choose a fiducial reduction factor $\mathbb{R} = 10^{-2}$ for all above runs, we investigate the reduced speed of light approximation with runs T1LR1, T1LR2.5 and T1LR3, which correspond

to $\mathbb{R} = 10^{-1}, 10^{-2.5}$ and 10^{-3} respectively. Moreover, T1L_HR1, T1L_HR2, T1L_LR1 and T1L_LR2 are runs to test the effects of spatial resolution compared to T1L, and T0.01L_HR and T0.01L_LR1 and T0.01L_LR2 are also carried out to compared to T0.01L. T1L_3D1 and T1L_3D2 are 3D runs with $\tau_* = 1$ and different resolutions. Next we introduce runs H1, H2 and H3.

2.6. Hot Wind vs. Radiation

Hot galactic winds may be driven by supernova explosions in star-forming and starburst galaxies (Chevalier & Clegg 1985). Besides radiation pressure on dust, it has been proposed that cold clouds may also be accelerated by ram pressure of the hot flow to observed velocities (Strickland & Stevens 2000; Murray et al. 2007; Cooper et al. 2008; Cooper et al. 2009; Fujita et al. 2009). However, recently both analytic calculations and numerical simulations shows that clouds are more likely to be quickly destroyed by shearing and Kelvin-Helmholtz instabilities before its fully acceleration to the velocity of the hot flow (Scannapieco & Brüggén 2015, Brüggén & Scannapieco 2016, Schneider & Robertson 2017; Zhang et al. 2017).

In this paper, we also compare the dynamics of cloud acceleration in the environment of hot wind and in an infrared radiation field. Heckman & Thompson (2017) estimate that the momentum injection rate of a hot wind is comparable to the expectation from radiation pressure in star-forming galaxies. We run simulations with a hot wind boundary condition to replace the radiation boundary. In order to compare to a fiducial radiation run, we set the momentum injection of hot wind $\rho_{\text{hot}} V_{\text{hot}}^2$ to be equal to the flux momentum F_*/c , where ρ_{hot} and V_{hot} are the density and velocity of the hot wind respectively. For simplicity, we do not adopt the widely used analytic models of hot wind given by Chevalier & Clegg (1985), but take Mach number of the hot wind $M_{\text{hot}} = V_{\text{hot}}/c_{s,\text{hot}}$ as a parameter. We set $M_{\text{hot}} = 5, 10$ and 20 , and the density of hot wind ρ_{hot} is given by

$$\rho_{\text{hot}} = \frac{F_*}{cV_{\text{hot}}^2} = \frac{a_r T_*^4}{\chi_0 c_{s,*}^2 M_{\text{hot}}^2}. \quad (22)$$

H1, H2, H3 in Table 1 show the initial conditions for the simulations of cloud in a hot flow. The cloud has an initial temperature $T_* = 100$ K, and density perturbation $\delta\rho/\rho$ is the same as in radiation runs, and the cloud is initially in thermal equilibrium with the hot medium with $\chi_0 = 10^4$. The lengthscale h_* for the cloud-hot flow runs are adjusted so that the initial column density of the cloud is exactly the same as that in radiation runs with $\tau_* = 1$. We find that $h_* = 2.8 \times 10^{-4}$ pc, 1.1×10^{-3} pc and 4.5×10^{-3} pc for H1, H2 and H3 respectively.

Some other runs are discussed in Section 4.

3. SIMULATION RESULTS

3.1. Large-Scale Runs: Optically Thin Case

We first run T0.01L, which corresponds to the large-scale run with $\tau_* = 0.01$. For simplicity, we assume the flux is constant along the vertical direction, and turn off the gravity. Figures 1 shows density and temperature snapshots from T0.01L. The cloud develops a significant “pancake” structure at $t \gtrsim 4 t_*$ elongated along the horizontal direction. The vertically upward radiation pressure on dust which accelerates the cloud and

the downward gas pressure from the background and the ram pressure due to the differential velocity between the front of the cloud and background combine together to squeeze the cloud along the vertical direction. Also, we find a downward “tail” structure forms at both sides of the cloud, which is caused by ram pressure of the hot background shearing the edge of the cloud. The lower panel of Figure 1 shows that the core of the cloud remains cold and dense during its acceleration. The interface between the front of the cloud and the background is heated to as high as $T/T_* \sim 10^5$ (i.e., $T \sim 10^7$ K). The low-density gas in the tails of the cloud behind the pancake structure is mixed up with gas temperature to $\sim 500 - 1000$ K, in which dust is sublimated. However, most mass of the cloud is still distributed in the pancake structure which is heated by radiation flux to a slightly higher temperature $T_c \sim 120$ K with $\rho \sim 1 - 50 \rho_*$. The irradiated cloud continues to be accelerated by radiation pressure on dust.

The upper panel of Figure 2 shows V_{mean} of the cloud in T0.01L. The cloud is almost linearly accelerated with time, suggesting that shredding and turbulence in the cloud has little impact on cloud acceleration. For an optically thin cloud, radiation flux penetrates the entire cloud without attenuation, the cloud can be accelerated uniformly as a whole, thus the cloud mean velocity can be simply estimated by

$$V_{\text{mean}} = \int \frac{\kappa F}{c} dt \sim V_* \left(\frac{\min\{T_c, 150\text{K}\}}{T_*} \right)^2 \left(\frac{t}{t_*} \right), \quad (23)$$

Note that the dust opacity is $\propto T_c^2$ at $T_c < 150$ K (equation 8), and becomes fairly flat at $150\text{K} < T_c < 1000$ K. Equation (23) gives a linearly increased V_{mean} with time t , where $V_* = \kappa_R F_* t_*/c = g_* t_*$ is the characteristic cloud velocity determined by the initial cloud temperature, radiation flux and the cloud characteristic lengthscale. Combining equations (9) and (10), we have $V_* \simeq 89 c_{s,*}$ for large-scale runs. Given $T_c \sim 120$ K in the cloud, we obtain $V_{\text{mean}} \sim 1.4 V_*(t/t_*)$ from equation (23), which is well consistent with the upper panel of Figure 1.

We stop the run at $t = 8t_*$ when the cloud reaches $V_{\text{mean}} \sim 10^3 c_{s,*}$ (~ 920 km s $^{-1}$). However, note that the assumption of a constant flux may break down if the flying distance of the cloud z_c is comparable to the size of the galaxy. The cloud flying distance z_c can be estimated by equation (21) that $z_c = 0.7 V_* t_*(t/t_*)^2 \simeq 6.2$ pc $(t/t_*)^2$. We have $z_c > R$ if

$$t > 5.7 t_* R_{200\text{pc}}^{1/2}, \quad (24)$$

with $R = 200$ pc $R_{200\text{pc}}$ being the size of the galaxy, thus the geometry of the galaxy becomes important to decelerated the cloud. In Section 4.4 we take into account the effect of gravity and varying flux along the height.

3.2. Large-Scale Runs: Optically Thick Case

We first perform the T1L run, which corresponds to the large-scale run with $\tau_* = 1$, and take T1L as the fiducial run. Figure 3 shows density and temperature snapshots from T1L. The cloud is initially similar to the case of T0.01L with a pancake structure elongated horizontally

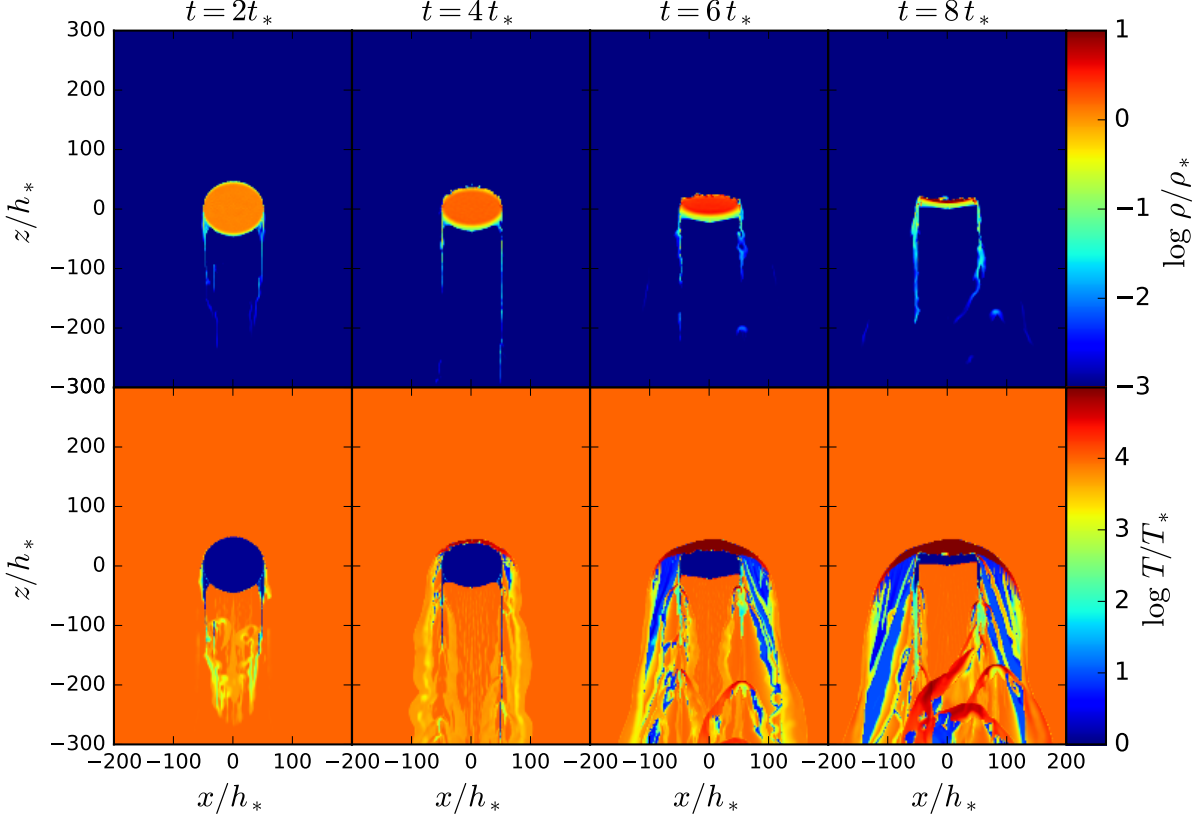


FIG. 1.— Density and temperature snapshots in run T0.01L, which is the large-scale (L) run with initial optical depth $\tau_* = 1$. The lengthscale in large-scale runs is $h_* = 0.1$ pc, and time unit $t_* \approx 1.1 \times 10^5$ yr (see equation 11).

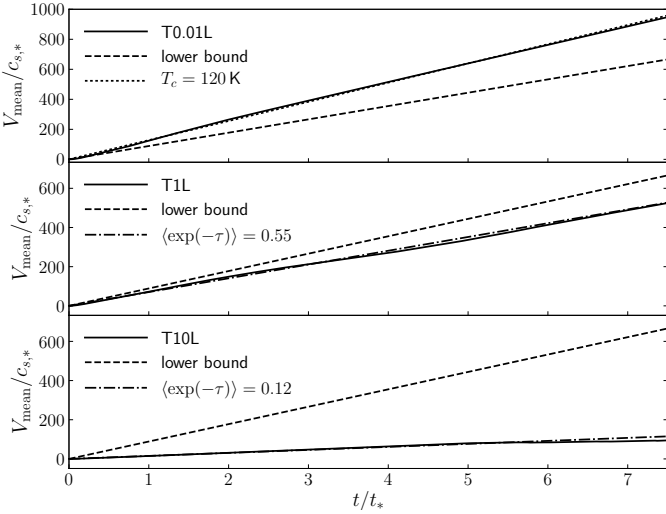


FIG. 2.— Cloud mean velocity V_{mean} for runs T0.01L, T1L and T10L, which correspond to large-scale runs with $\tau_* = 0.01, 1$ and 10 respectively. The lower bound (dashed lines) for *optical thin cloud* acceleration is given by equation (23). The fitting line in upper panel is also given by equation (23) with $T_c = 120$ K, and the fitting lines in middle and lower panels are given by equation (25) with the averaged attenuation factor $\langle e^{-\tau} \rangle = 0.55$ and 0.12 respectively.

and long tails behind the cloud at $t = 1.5t_*$. However, the evolution of the irradiated cloud becomes quite different from T0.01L at late time. The cloud has optical depth $\tau_* = 1$ along the vertical diameter, but the optical depth is lower at the outside region of the cloud. Since the radiation flux is attenuated by a factor of $e^{-\tau}$ and

distributed inhomogeneously inside the cloud, the cloud can no longer be accelerated uniformly as a whole. Different radiation force due to different flux inside the cloud produced a shear in the cloud – the outside region of the cloud at both sides is accelerated faster than the center of the cloud. Most mass with lower velocity is dragged behind and accumulated at the bottom of the cloud. The differential velocity between the cloud outside and central regions eventually stretches out the cloud, leading to a filamentary structure elongated along the vertical direction. The gas in the filamentary structure is much denser than the outside region of the cloud. We find that the peak value of density in the central region increases to $\rho \sim 10 - 20\rho_*$ at $t = 4.5t_*$ and slightly decreases to $\rho \sim 1 - 10\rho_*$ at $t = 6t_*$.

We also carry out other two large-scale runs T3L ($\tau_* = 3$) and T10L ($\tau_* = 10$). The mean velocity for optically thick cloud can be estimated by

$$V_{\text{mean}} \sim V_* \langle e^{-\tau} \rangle \left(\frac{\min\{T_c, 150 \text{ K}\}}{T_*} \right)^2 \left(\frac{t}{t_*} \right), \quad (25)$$

where $\langle e^{-\tau} \rangle = \int \rho e^{-\tau} dt dV / M_c t$ is the mass and time averaged attenuation factor, which measures the impact of optical depth on cloud acceleration. The middle and lower panels in Figure 2 shows V_{mean} from two runs T1L and T10L. We find that $T_c \sim 120$ K still holds for optically thick clouds. The values of V_{mean} can be approximately given by $\langle e^{-\tau} \rangle \simeq 0.55$ in equation (25) for T1L and $\langle e^{-\tau} \rangle \simeq 0.12$ for T10. Also, from T3L we find that $\langle e^{-\tau} \rangle \simeq 0.31$ for $\tau_* = 3$, which is the intermediate case

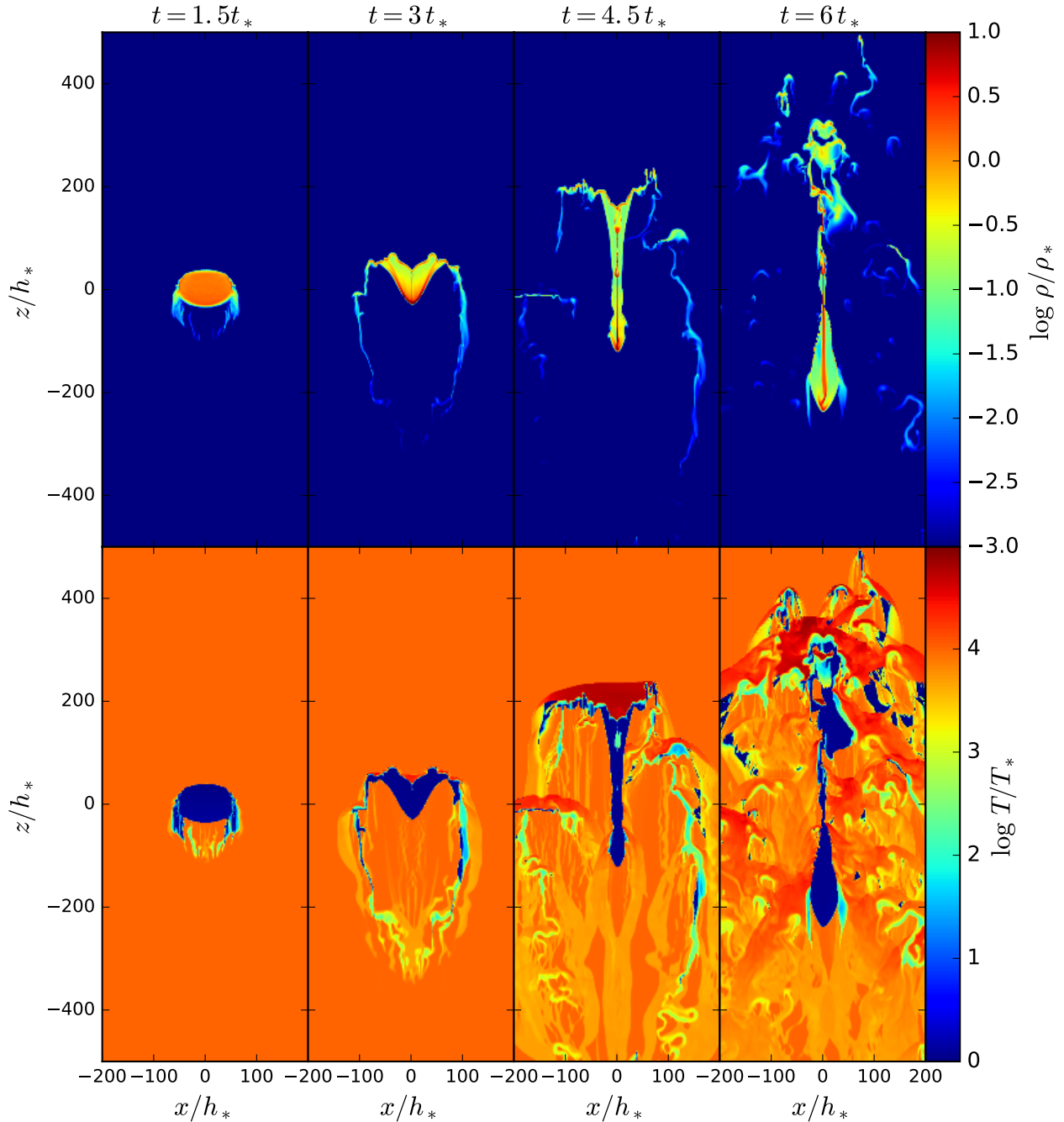


FIG. 3.— Density and temperature snapshots in run T1L, which is the large-scale run with $\tau_* = 1$. The lengthscale h_* and time unit t_* are the same as in Figure 1.

between T1L and T10L. Combining results from T1L to T10L, we give an empirical formula to fit the attenuation factor that

$$\langle e^{-\tau} \rangle = \exp(0.92 - 1.5\tau_*^{0.3}), \quad (26)$$

which holds for $\tau_* \geq 1$. If we combine $\epsilon = \langle e^{-\tau} \rangle (T_c/T_*)^2$ as a new parameter and $V_c = \epsilon V_*(t/t_*)$ for both optically thin and optically thick clouds, we obtain

$$\epsilon \simeq \min\{1, \exp(1.3 - 1.5\tau_*^{0.3})\}, \quad (27)$$

higher τ_* gives a slower acceleration.

Figure 4 shows snapshots of density and z -component

radiation flux F_{rz} for T1L, T3L and T10L at a same time $t = 6t_*$. T3L also shows a clear filamentary structure stretched vertically, which is similar as in T1L. Cloud in T10L has the largest initial optical depth, radiation only blows away the outside region of the cloud at $t = 6t_*$, but the core of the cloud is moving slowly. We find that a filamentary structure is eventually formed at $t \sim 8t_*$ in T10L. Furthermore, the flux F_{rz} is mainly attenuated in the densest region of the cloud and decreases to $F_{rz} \sim 0.1F_{r,*}$ in the bottom of the cloud in T3L, and $F_{rz} \sim 0$ in T10L. On the contrary, we find that F_{rz} in the run for optically thin cloud T0.01L is uniform

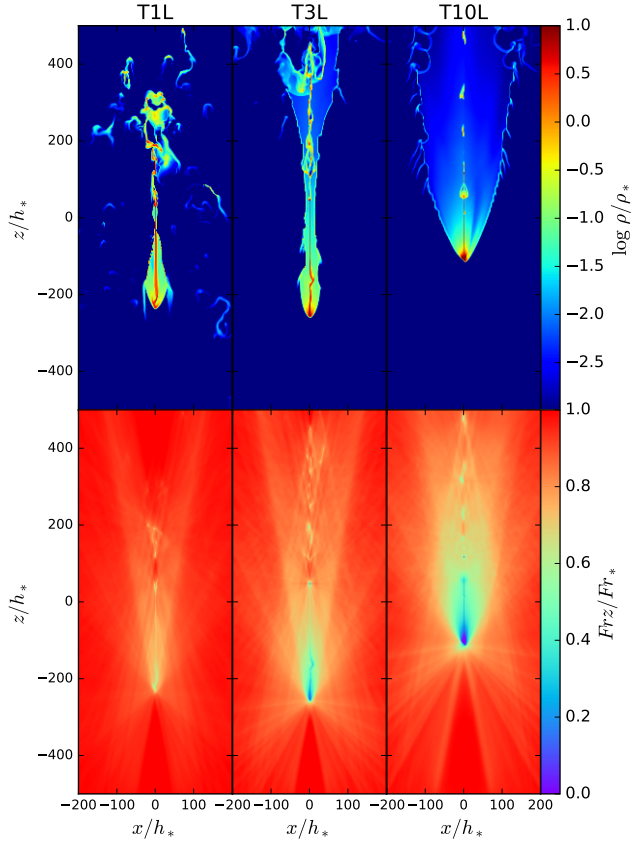


FIG. 4.— Density and z -component flux F_{rz} snapshots from runs T1L, T3L and T10L at $t = 6t_*$.

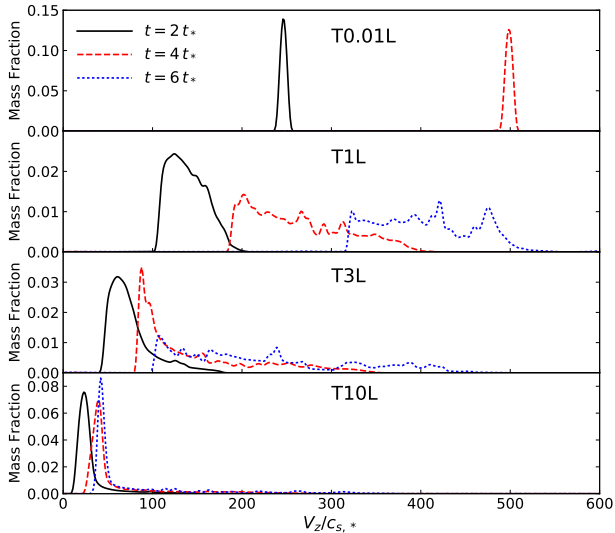


FIG. 5.— Velocity probability distribution function (PDF) for runs T0.01L, T1L, T3L and T10L at $t = 2t_*$, $4t_*$ and $6t_*$.

with $F_{rz} \simeq F_{r,*}$ everywhere. Higher optical depth means heavier flux attenuation inside the cloud. Note that this result is in contrast to the dusty shell acceleration (e.g., Krumholz & Thompson 2012, 2013; Davis et al. 2014; Zhang & Davis 2017), in which higher shell optical depth leads to a higher acceleration. The key difference between them is that the radiation flux can be well trapped

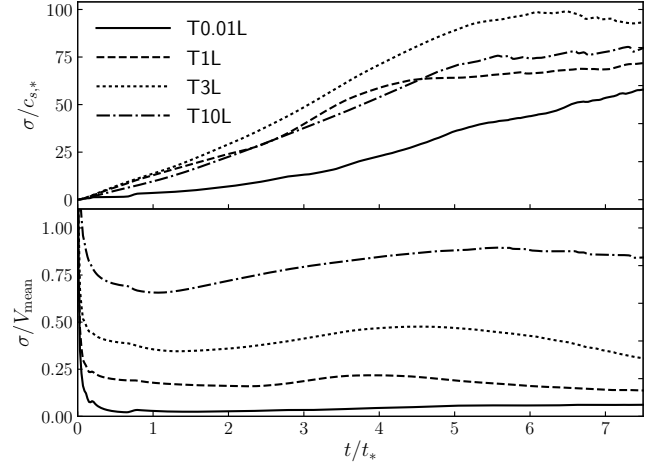


FIG. 6.— Velocity dispersion in the clouds $\sigma/c_{s,*}$ (upper panel) and the ratio σ/V_{mean} for runs T0.01L, T1L, T3L and T10L.

inside a shell and the momentum coupling between the radiation field and the shell correlates with the shell optical depth, but the flux can easily escape from a cloud. As shown in Figure 4, the re-radiated flux from the cloud escapes away from the cloud, although the re-radiated flux profiles show a phenomena referred to as “ray-effects”, which correspond to unphysical anisotropies in the radiation field due to the angular resolution. Ray-effects have been discussed in the literature (e.g., Larsen & Wolhaber 2008; Finlator et al. 2009). The effects of angular resolution were explored in the appendix of Davis et al. (2014) in which the convergence was found even when ray-effects were presented.

It is also important to study the spread/dispersion of velocities about the mean velocities for the clouds. Figure 5 compares mass-weighted velocity probability distribution functions (PDFs) in the vertical direction for four runs from T0.01L to T10L. The PDFs for all runs shift to higher velocity of v_z , but the cloud with lowest optical depth $\tau_* \ll 1$ gains the highest acceleration but the tightest extension of velocities. This is consistent with the result that optically thin cloud is accelerated as a whole. The velocity distribution becomes more extended in T1L with time, and v_z spreads from $V_z \sim 320 c_{s,*}$ to $\sim 550 c_{s,*}$ at $t = 6t_*$. The velocity distribution becomes even more extended in T3L at $t = 6t_*$, from $V_z \sim 100 c_{s,*}$ to $\sim 450 c_{s,*}$ at $t = 6t_*$. The shape of the PDF for T10L is somewhat similar to T0.01L, however, T10L shows a slowest cloud acceleration, and the PDF of T10L shows a tailed profile extending to $V_z \sim 300 c_{s,*}$. A fraction of the cloud in T10L has been already accelerated to a high velocity, while the main body still remains a low velocity.

Another quantity to measure the cloud velocity spread or turbulence is the mass weighted velocity dispersion of the cloud σ , which is given by

$$\sigma_i^2 = \frac{1}{M} \int \rho (v_i - \langle v_i \rangle)^2 dV, \quad (28)$$

where i has x and z components for 2D runs, and x, y, z components for 3D runs, and the total velocity dispersion is $\sigma = \sqrt{\sum \sigma_i^2}$. Figure 6 shows the properties of velocity dispersion in four runs. We find that T3L shows the largest velocity dispersion that $\sigma \sim 100 c_{s,*}$ at $t = 6.5t_*$, while σ in T1L is comparable to that in T3L, and T10L

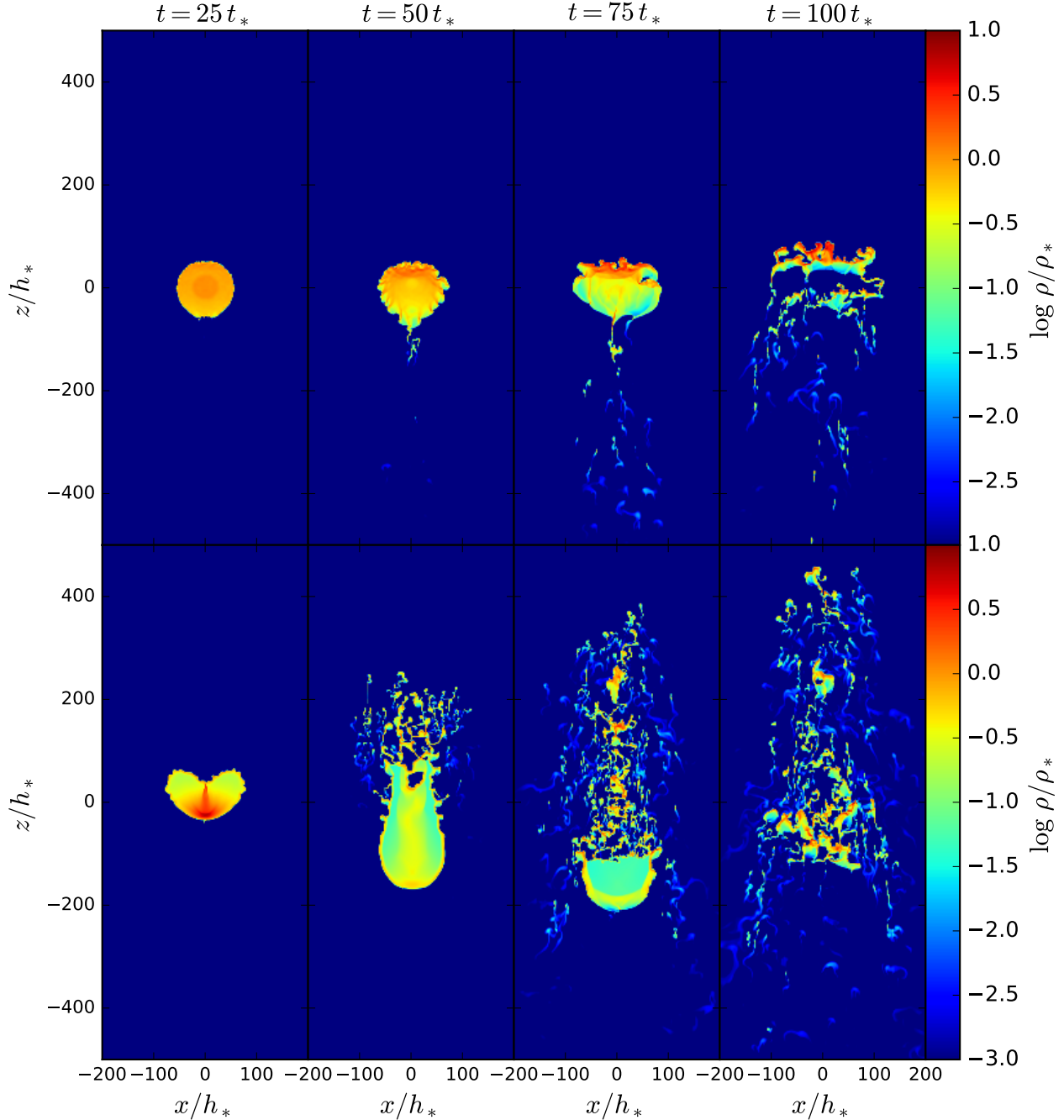


FIG. 7.— Density snapshots in runs T0.01S (upper panels) and T1S (lower panels), which are the small-scale (S) runs with $\tau_* = 0.01$ and 1 respectively. The lengthscale for small-scale runs is $h_* = c_{s,*}^2/g_*$, and the time unit $t_* \approx 1.2 \times 10^3$ yr (see equations 10 and 12).

shows a lower σ compared to T3L, while T0.01L gives the lowest σ . These results are consistent with Figure 5. The lower panel of Figure 6 shows that σ is small compared to V_{mean} , except for T3L which gives $\sigma \gtrsim 0.75V_{\text{mean}}$ after $t \gtrsim 3t_*$.

3.3. Small-Scale Runs

As mentioned in Section 2.2, the consideration to resolve the scale of gas turbulence motivates the small-scale runs. We carry out two runs T0.01S and T1S, which are compared to the large-scale runs T0.01L and T1L respectively. In small-scale runs we fix the column density of

the cloud the same as that in the corresponding large-scale runs in cgs units, but shrink the cloud radii to $50h_*$ with $h_* = c_{s,*}^2/g_*$. The ratio of the the initial average density of the cloud and the unit of time t_* in small-scale (equation 12) and large-scale runs (equation 11) satisfies

$$\frac{\rho_*^S}{\rho_*^L} = \frac{t_*^L}{t_*^S} = \frac{h_*^L}{h_*^S} \simeq 89T_{*,2}^5, \quad (29)$$

where $T_{*,2} = T_*/100$ K. The density of cloud as well as the background in small-scale runs increase about two orders of magnitude compared to the large-scale runs.

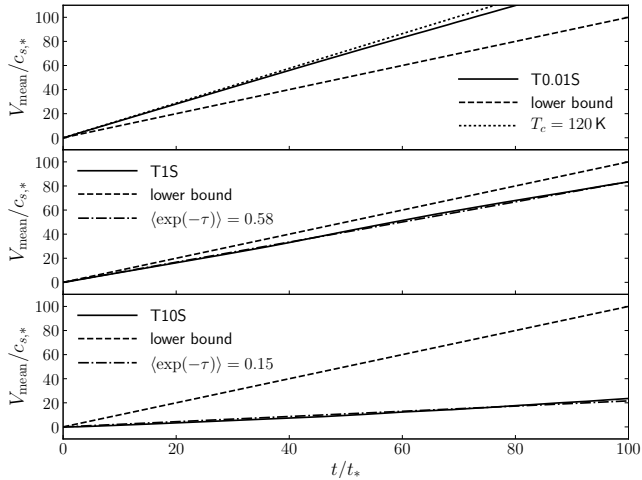


FIG. 8.— Cloud mean velocity V_{mean} for runs T0.01S (upper panel), T1S (middle panel) and T10S (lower panel), which correspond to the small-scale runs with $\tau_* = 0.01, 1$ and 10 respectively. The lower bound (dashed lines) for *optical thin cloud* acceleration is given by equation (23), also the lines denoted by $\langle \exp(-\tau) \rangle$ are plotted based on equation (25).

The dimensionless equations under code units for small-scale runs are almost the same as for the large-scale runs, except for one single parameter \mathbb{P} , which measures the relative importance of radiation pressure over gas pressure (see Section 2.4). Mathematically the difference between large-scale and small-scale runs are caused by \mathbb{P} . A lower \mathbb{P} gives a slower acceleration and less pressure on the cloud. We have $\mathbb{P} \simeq 8.9 \times 10^3 \tau_*^{-1}$ for large-scale runs and $\mathbb{P} \simeq 1.0 \times 10^2 \tau_*^{-1}$ for small-scale runs.

Figure 7 shows density snapshots from T0.01S (upper panels) and T1S (lower panels). We stop simulations at $t = 100 t_*$, which in cgs units is still shorter than $8 t_*$ in large-scale runs, but the behavior of the cloud can be already well observed within $t \lesssim 100 t_*$ in small-scale runs. The cloud in T0.01S is squeezed by radiation pressure and background pressure, and forms a weak pancake structure at $t \sim 75 t_*$. However, since \mathbb{P} is lower, the dimensionless density ρ/ρ_* is also lower in T0.01S than that in T0.01L, and the cloud region near the background with lower ρ/ρ_* is more likely to occur shearing instability. A Rayleigh-Taylor-like instability is developed at the front of the cloud interacting with the background, while the velocity difference between the cloud and the background at both sides of the cloud eventually shreds the cloud at $t \sim 90 - 100 t_*$. On the other hand, in T1S a vertically elongated structure emerges by $t = 50 t_*$, while Kelvin-Helmholtz instability occurs at both sides of the cloud. In contrast to the filamentary structure in T1L, the interaction between the relatively low-density front of the elongated structure and the background fragments the front of the cloud into many small clumps. The cloud is eventually shredded by background pressure at $t \sim 100 t_*$ and fragments into pieces.

Although the cloud morphology in small-scale runs is significantly different from that in large-scale runs, we find that the bulk acceleration of the cloud shows similar behavior. Figure 8 shows V_{mean} for T0.01S, T1S and T10S. We find that equations (23) and (25) can also be applied for small-scale runs with $V_* \simeq c_{s,*}$, and the temperature of the cloud is still $T_c \sim 120 \text{ K}$, thus $V_{\text{mean}} \sim 1.4 V_*(t/t_*)$ also holds for T0.01S. Also, we ob-

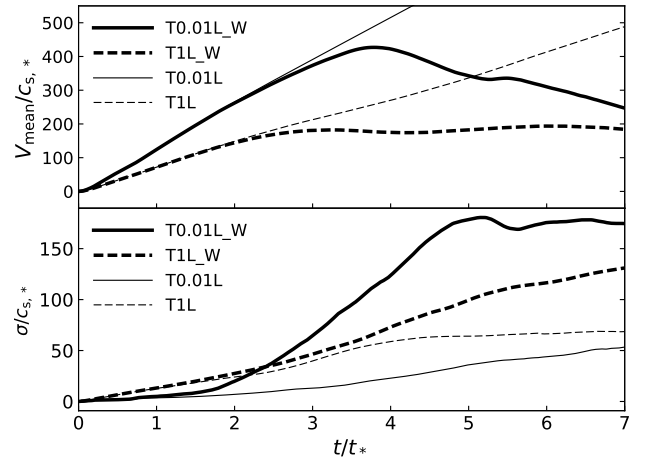


FIG. 9.— Cloud mean velocity V_{mean} (upper panel) and velocity dispersion σ (lower panel) for the runs T0.01L_W and T1L_W compared to T0.01L and T1L. Here T0.01L.W and T1L.W are the large-scale runs with a warm background (W) setup $\chi_0 = 10^2$.

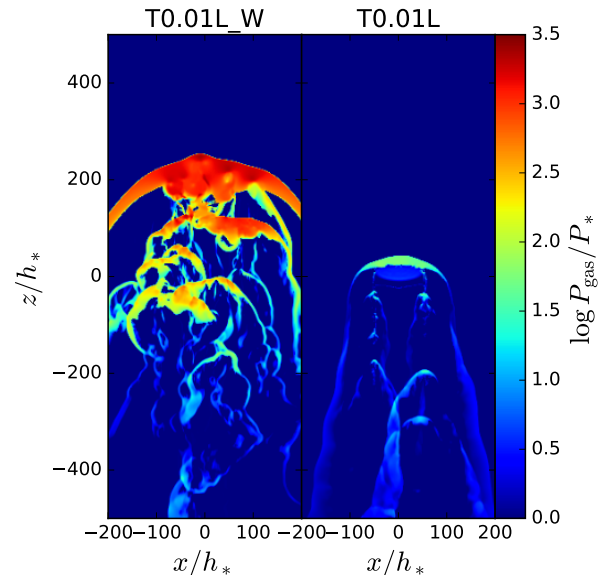


FIG. 10.— Comparison of thermal pressure in T0.01L.W and T0.01L at $t = 6 t_*$. Here $P_* = \rho_* c_{s,*}^2$ is the unit of pressure and P_{gas}/P_* is the dimensionless pressure.

tain $\langle e^{-\tau} \rangle \simeq 0.57$ for T1S, and $\langle e^{-\tau} \rangle \simeq 0.14$ for T10S, which shows similar results compared to T1L and T10L respectively. Equation (27) still roughly holds for cloud acceleration from $\tau_* = 1$ to $\tau_* = 10$. Changing the characteristic lengthscale of cloud may change the cloud morphology, but does not change cloud acceleration.

3.4. Warm Background Medium

So far we discuss clouds in a hot background medium with density ratio $\chi_0 = 10^4$. Here we consider clouds in a warm background where has a temperature of $T_{\text{bgd}} = 10^4 \text{ K}$ and $\chi_0 = T_{\text{bgd}}/T_* = 10^2$. Since thermal pressure and ram pressure from the warm background are significantly stronger than those from the hot background, the interaction between the cloud and the background may cause different behavior in contrast to the cloud in a hot background. We carry out two runs T0.01L_W and

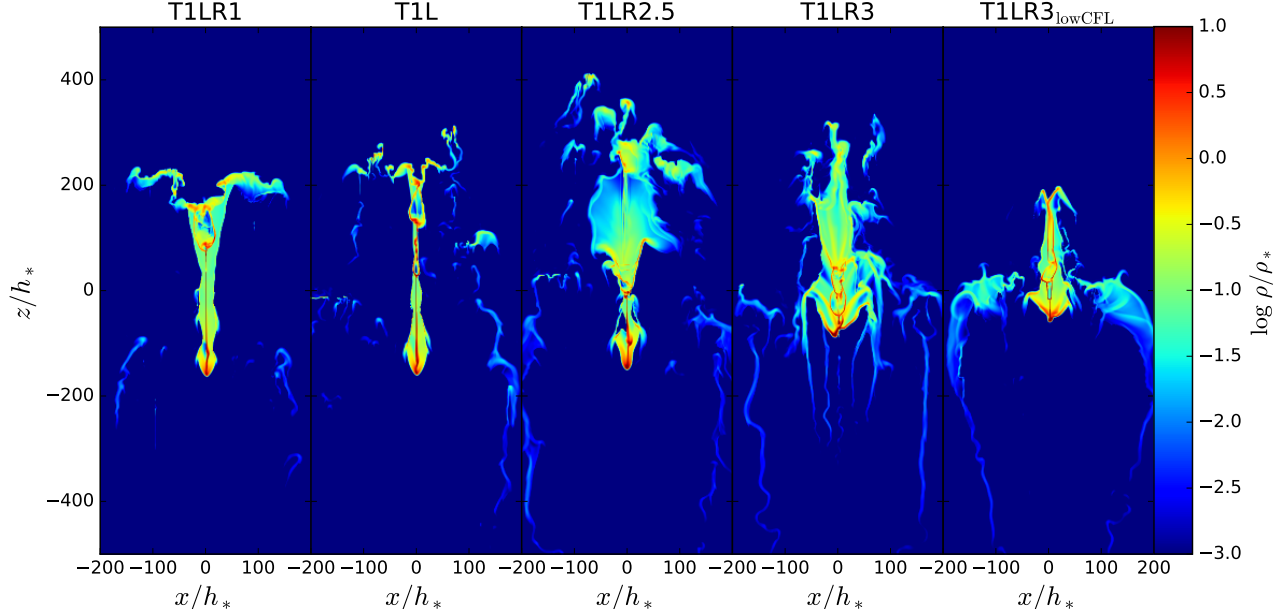


FIG. 11.— Comparison of density profiles from runs with different reduced speed of light at $t = 5t_*$, where T1LR1, T1L, T1LR2.5 and T1LR3 correspond to large-scale runs with the reduction factor $\mathbb{R} = 10^{-1}$, 10^{-2} , $10^{-2.5}$ and 10^{-3} respectively. The TLR3_{lowCFL} run has a lower CFL number so the timestep is exactly the same as in T1L.

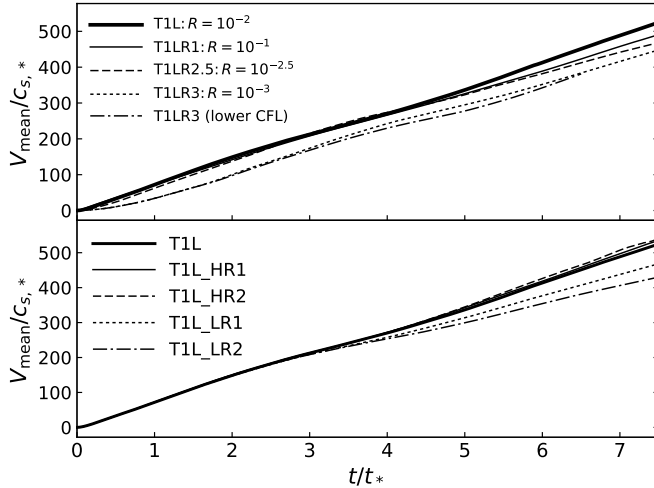


FIG. 12.— Cloud mean velocities for different reduced speed of light T1L, T1LR1, T1LR2.5 and T1LR3 (upper panel), and different spatial resolution T1L, T1L_HR1, T1L_HR2, T1L_LR1 and T1L_LR2 (lower panel), where the definitions of “HR1”, “HR2”, “LR1” and “LR2” are given in Table 1.

T1L_W to study the impact of denser background. Figure 9 shows V_{mean} and σ for these two runs which are compared to T0.01L and T1L respectively. In contrast to T0.01L and T1L, the mean velocity of the cloud in T0.01L_W increases to $V_{\text{mean}} \sim 420 c_{s,*}$ at $t \simeq 3.8t_*$, then the cloud begins to be decelerated, while V_{mean} in T0.01L_W stays flat at $V_{\text{mean}} \sim 180 - 190 c_{s,*}$ for $t \gtrsim 3t_*$. The lower panel in Figure 9 shows that the velocity dispersions in T0.01L_W and T1L_W are also significantly larger than T0.01L and T1 respectively. In particular, the velocity dispersion is comparable to mean velocity V_{mean} at $t \sim 7t_*$ in T0.01L_W, because the cloud becomes very turbulent and is eventually mixed up with the background.

We find that thermal pressure in the shock-like interface between the front of the cloud and background dom-

inates over ram pressure from the background. In other words, thermal pressure plays more important role to re-shaping and decelerating the cloud. Figure 10 shows thermal pressure P_{gas}/P_* in T0.01L_W and T0.01L at $t = 6t_*$. Note that the high pressure region in Figure 10 is not in the cloud, but in the interface region between the cloud and non-disrupted background. We find that the temperature in the shocked interface between the cloud and background is $T \sim 10^4 T_*$ in T0.01L_W, while $T \sim 10^5 T_*$ in T0.01L, thus the interface gas pressure reaches $P_{\text{gas}} \sim 10^3 P_*$ in T0.01L_W, while $P_{\text{gas}} \sim 50 P_*$ in T0.01L, which is one and half order of magnitude lower compared to the warm background. The high gas pressure acting on the cloud from the interface eventually prevents the cloud from being accelerated by radiation, and shreds the cloud more quickly than the cloud in a hotter and more tenuous background.

Another important quantity to measure the cloud properties is the cloud survival time, which is investigated in Section 4.1. Also cooling and heating in the ionized background can change the cloud dynamics and morphologies, which is discussed in Section 4.2. Before discussing them we study the effects of some simulation parameters such as reduced speed of light, resolution and simulation dimensionality in the following several sections.

3.5. Reduced Speed of Light Approximation

The details of the reduced speed of light approximation are discussed in Appendix A. Clouds in large-scale runs has a maximum velocity $v_{\text{max}} \sim 500 - 10^3 c_{s,*}$ and optical depth $\tau_{\text{max}} \sim 1$, thus we have the constraint $500 - 1000 \ll \tilde{C} \ll C$ using the criterion equation (A2) in Appendix A. The lower bound of the reduction factor is $\mathbb{R} = C/\tilde{C} \gg 1.5 - 3 \times 10^{-3}$. Therefore it is justified to use $\mathbb{R} = 10^{-2}$ as a fiducial value in the paper. We take T1L as a fiducial run and perform other three runs with various reduction factor \mathbb{R} that T1LR1 ($\mathbb{R} = 10^{-1}$),

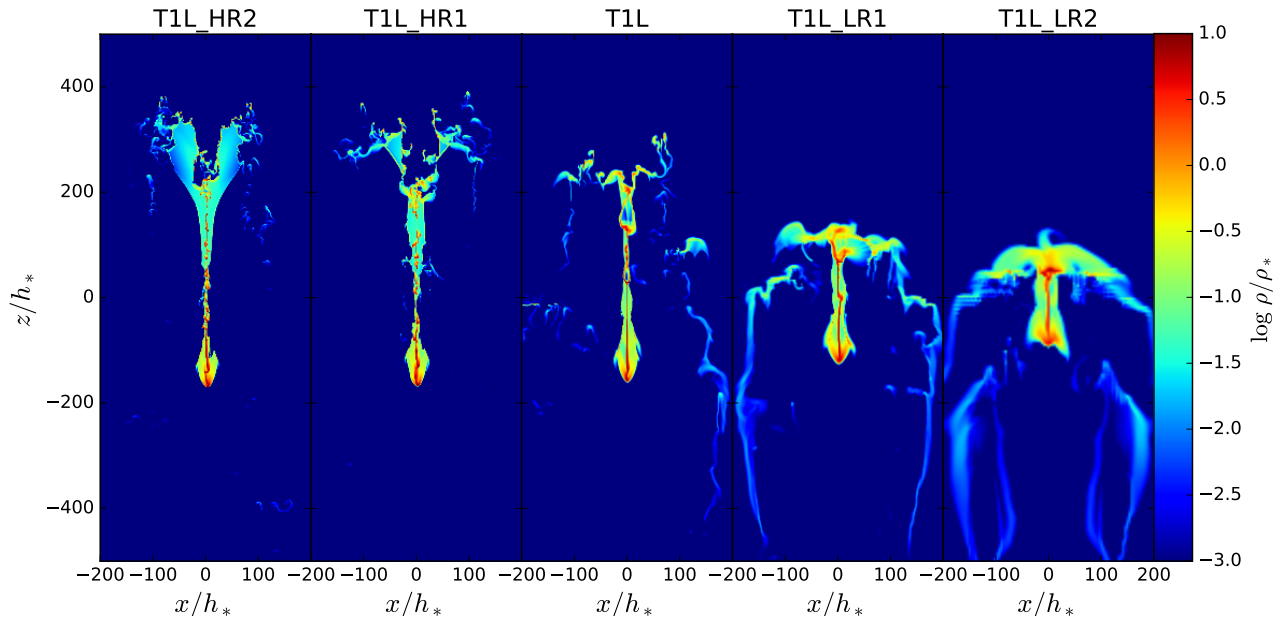


FIG. 13.— Comparison of runs for various spatial resolutions T1L_HR2, T1L_HR1, T1L, T1L_LR1, T1L_LR2 at $t = 5t_*$.

T1LR2.5 ($\mathbb{R} = 10^{-2.5}$) and T1LR3 ($\mathbb{R} = 10^{-3}$) to investigate the effects of \mathbb{R} . The left four panels of Figure 11 compares the cloud density profiles for varying \mathbb{R} at $t = 5t_*$. The cloud morphologies are similar in T1LR1 and T1L, while the filamentary structure slightly changes in T1LR2.5 and becomes less vertically extended in T1LR3. We also find that velocity dispersion varies for different \mathbb{R} , which result is consistent with Figure 11 that the shape and properties of turbulence depends on \mathbb{R} . However, most of the cloud mass is still accumulated in the lower region of the cloud along the vertical direction, and cloud acceleration which mainly depends on the bottom region of the cloud does not change significantly. The upper panel of Figure 12 shows V_{mean} for these runs. We find that V_{mean} does not change obviously for $\mathbb{R} \geq 10^{-2.5}$. Even $\mathbb{R} = 10^{-3}$ gives less than $\sim 20\%$ difference in V_{mean} . Thus we conclude that $10^{-3} \lesssim \mathbb{R} \lesssim 1$ gives a good approximation for cloud acceleration.

A higher \mathbb{R} gives a smaller timestep in simulations. So far in all 2D simulations we choose the Courant–Friedrichs–Lewy (CFL) number to be 0.4 (see Appendix A), it is worthwhile to test whether it is equivalent to use a lower CFL number instead of a higher \mathbb{R} to decrease the timestep, or \mathbb{R} is more important to affect the RT. We perform another T1LR3 run (T1LR3_{lowCFL}) with $\mathbb{R} = 10^{-3}$ but has a smaller CFL number so the timestep is exactly the same as in T1L. The rightmost panel of Figure 11 shows that the geometry of the cloud in T1LR3_{lowCFL} is more like that in T1LR3 rather than in T1L, and the upper panel of Figure 12 shows that the cloud velocity for T1LR3_{lowCFL} is almost identical to that for T1LR3. From the aspect of cloud evolution, we conclude that varying \mathbb{R} is more important to affect the properties of RT equation rather than to vary timestep in hydrodynamic equations.

We also test the reduction factor in small-scale runs. Note that v_{max} is much lower in small-scale runs, equation (A2) gives a much lower estimate on the lower bound of \mathbb{R} that $\mathbb{R} \gg 1.5 \times 10^{-4}$ for $v_{\text{max}} \sim 100 c_{s,*}$. However, we find that even $\mathbb{R} = 10^{-4}$ gives an good approxima-

tion of both V_{mean} and velocity dispersion σ compared to higher \mathbb{P} . We report that the small-scale runs allow a much weaker constraint on \mathbb{P} .

3.6. Dependence on Spatial Resolution

We also study the impact of spatial resolution on cloud simulations. The fiducial run T1L assumes that $\Delta z/h_* = 1$ (see Table 1). Compared to the fiducial run, a number of other runs are also performed here, with higher resolutions $\Delta z/h_* = 0.5$ (T1L_HR1), $\Delta z/h_* = 0.25$ (T1L_HR2), and lower resolutions $\Delta z/h_* = 2$ (T1L_LR1) and $\Delta z/h_* = 4$ (T1L_LR2).

Figure 13 compares density snapshots from five runs with various resolutions at $t = 5t_*$. The shapes of the cloud are obviously different in the low-resolution runs from the high-resolution runs. In general, higher spatial resolution run gives a longer stretched cloud along the vertical direction. More specially, we find that the resolution in z -direction controls the behavior of the cloud. Same resolution in x -direction but higher resolution in z -direction (e.g., T1L_HR2 compared to T1L_HR1) gives a more rapidly evolved cloud with higher turbulence, while we also test that different x -direction but same z -direction resolution shows similar cloud evolution. A lower z -direction resolution makes cloud more compact along the vertical direction. In spite of these differences, the filamentary structure still appears in all the runs, with most mass distributed at the bottom of the clouds. The lower panel of Figure 12 shows V_{mean} with various resolution runs. The cloud bulk acceleration V_{mean} is almost identical from the highest resolution run T1L_HR2 to the moderate resolution run T1L, which shows that T1L is justified as a fiducial resolution. Lower resolution runs show slower acceleration, but the difference is within $\sim 20\%$ between T1L and the lowest-resolution run T1L_LR2, which means that V_{mean} only depends weakly on spatial resolution.

On the other hand, we find that the impact of spatial resolution is much less important for optically thin cloud. We carry out two large-scale runs T0.01L_HR1,

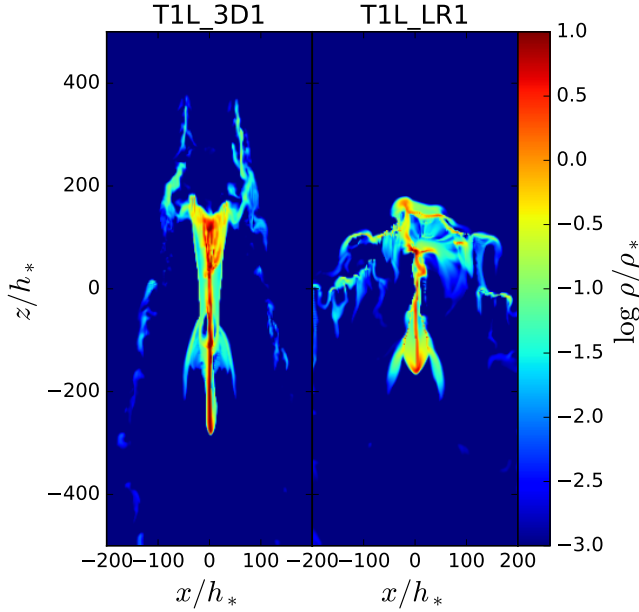


FIG. 14.— Comparison of density profiles from 3D run T1L_3D1 and 2D run T1L_LR1 at $t = 6 t_*$. The 2D xz slice with $y = 0$ is plotted for the 3D panel.

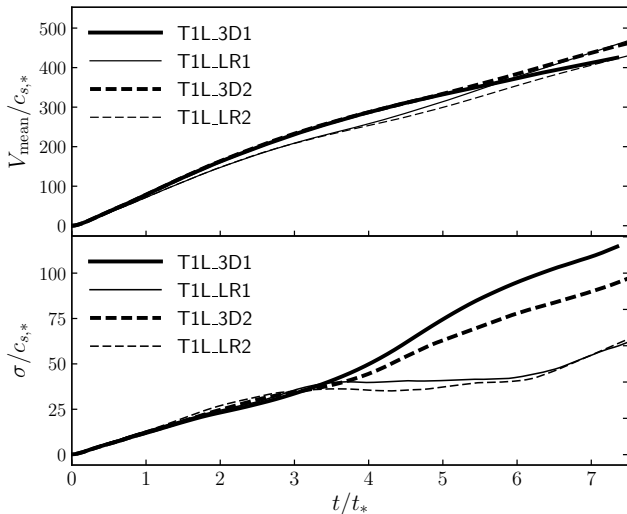


FIG. 15.— Cloud mean velocities (upper panel) and velocity dispersion (lower panel) for the 3D runs T1L_3D1 and T1L_3D2, and the equivalent 2D runs T1L_LR1 and T1L_LR2.

T0.01L_LR1 as shown in Table 1) and compare to T0.01L, but find almost no difference of V_{mean} among them. Since the acceleration depends on $\kappa F/c$, which is almost uniformly distributed inside the cloud both for lower and higher-resolution runs, the evolution of the cloud is very similar in runs with different resolutions.

3.7. 3D Simulations

So far we discuss the simulation results based on 2D simulations, but 3D simulation may change some properties of the cloud. Optically thick cloud develops non-linear structure which may be different in 2D and 3D simulations. Since 3D runs are more expensive than 2D runs, we only carry out two runs: T1L_3D1 and T1LR2_3D2, which are equivalent to T1L_LR1 and T1L_LR2 runs in

2D with the same spatial resolution respectively. We set the CFL number to be 0.3 in 3D runs, thus the time-steps in 3D runs are relatively smaller compared to the 2D runs with the same spatial resolution. In Section 3.6 we show that although the cloud morphologies vary for different resolution, the cloud bulk acceleration is still similar. Therefore it is justified to adopt low-resolution 2D runs and see the difference of cloud evolution with an extra dimension.

Figure 14 compares density distribution in T1L_3D1 with T1L_LR1 at a same time $t = 6 t_*$. Two runs show a bit different cloud evolution. The behavior of the cloud is more like T1L rather than T1L_LR1. The 3D cloud is stretched out and elongated along the vertical direction from $z \sim -300 h_*$ to $200 h_*$, which shape is similar to T1L and other 2D higher resolution runs. Also the filamentary structure in T1L_3D1 has a typical value of $\sim 5 - 10 \rho_*$, which is slightly denser compared to the cloud in T1L_LR1, but is comparable to T1L. In spite of the difference, we find that the values of V_{mean} do not change too much in these runs. The upper panel of Figure 15 shows that the difference of V_{mean} between 2D and 3D runs is less than $\sim 10\%$. The lower panel of Figure 15 shows that velocity dispersion of the cloud can significantly increase to $\sigma \sim 120 c_{s,*}$, which means that 3D cloud is more turbulent than 2D cloud. The comparison suggests that 2D runs are good approximations to model cloud acceleration, although the detailed geometry and turbulence of the clouds depend on the dimensionality of runs.

4. DISCUSSION

4.1. Cloud Survival Time

We follow Scannapieco & Brüggén (2015) and Schneider & Robertson (2017) to define the cloud mass as the summation of all gas denser than $1/3$ of the initial cloud mean density ρ_* . Figure 16 shows the cloud mass evolution, i.e., the ratio of the cloud mass to the initial cloud mass $M_c/M_{c,i}$ as a function of time, for large-scale runs in the hot ($\chi_0 = 10^4$) and warm ($\chi_0 = 10^2$) background, and for small-scale runs. In large-scale runs an optically thin cloud in the hot background ($\tau_* = 0.01$ and $\chi_0 = 10^4$) shows the most ideal acceleration, in which the mass of cloud is almost unchanged during its acceleration. In the warm background a same optically thin cloud is decelerated by thermal pressure of the background at $t \sim 3.8 t_*$ (see Figure 9), meanwhile the cloud begins to be shredded, and $M_c/M_{c,i}$ quickly drops from $M_c/M_{c,i} \sim 0.9$ to ~ 0.5 at $t \sim 7 t_*$. For large-scale runs with $\tau_* = 1$, about $\sim 70\% - 75\%$ of the initial mass is still in the cloud at $t = 7 t_*$, while the mass fraction $M_c/M_{c,i}$ drops to $\sim 50\%$ in the case of warm background, slightly lower than that in a hot background, but similar to the optically thin cloud in the warm background. On the other hand, the evolution of cloud mass in small-scale runs show an interesting behavior. The cloud mass fraction drops to $M_c/M_{c,i} \sim 0.5$ at $t \sim 50 t_*$ in T1SR2, but the mass fraction increases again afterwards. Figure 7 and the right panel of Figure 16 shows that the cloud is initially stretched and the cloud density drops until $\sim 50 t_*$ when the cloud starts to fragments into pieces. The density of many fragmentations increases again up to $\rho \sim \rho_*$ because the pressure of the back-

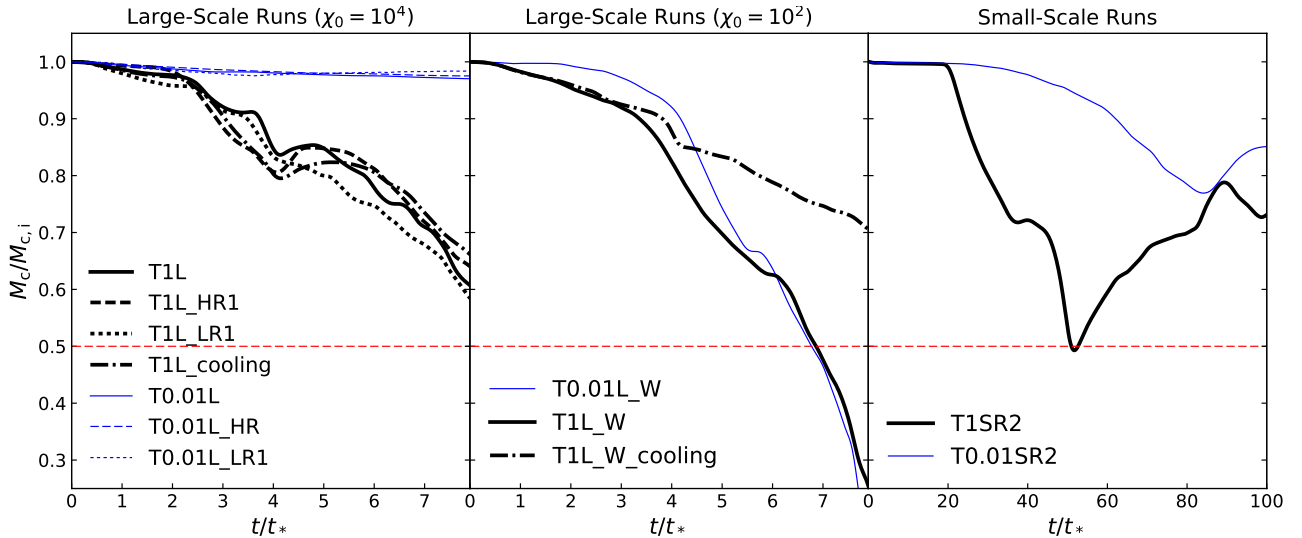


FIG. 16.— Evolution of cloud mass, which is calculated as the sum of all gas in the simulation with a density greater than $1/3$ the initial median density, for large-scale runs in hot background ($\chi_0 = 10^4$, left panel), warm background ($\chi_0 = 10^2$, middle panel), and small-scale runs (right panel). The runs in left panel are from Sections 3.1, 3.2, 3.6, runs in middle panel are from Section 3.4, and runs in right panel are from 3.3.

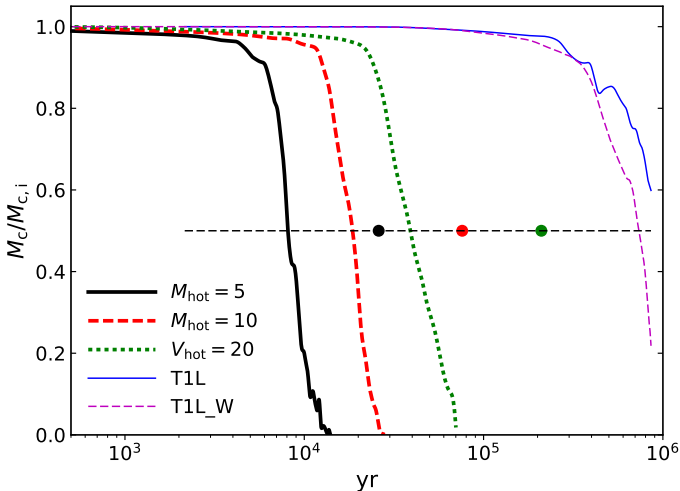


FIG. 17.— Mass evolution of cloud accelerated by hot wind runs H1, H2 and H3 with hot flow Mach number $M_{\text{hot}} = 5, 10, 20$ respectively, and radiatively accelerated runs T1L and T1L_W for comparison. Three dots from left to right are the values of t_{50} given by equation (30) for $M_{\text{hot}} = 5, 10, 20$ respectively.

ground confines and squeezes these small pieces. Then $M_c/M_{c,i}$ rises up again to $M_c/M_{c,i} \sim 0.8$. A similar behavior also emerges in T0.01S, in which the mass of the cloud drops to $M_c/M_{c,i} \sim 0.7$ at $t \sim 80t_*$ and increases again afterwards. We do not find significant decrease of $M_c/M_{c,i}$ below 0.5 for $t \lesssim 100t_*$.

If we define the cloud survival time as the time when $M_c/M_{c,i}$ drops to 0.5, and denote it as t_{50} (see Scannapieco & Brüggén 2015), we find that t_{50} mainly depends on τ_* and χ_0 . The cloud survival time t_{50} is longer than the simulation time in runs with $\chi_0 = 10^4$ both for large-scale and small-scale runs, while the cloud survival time is significantly shorter in the warm background $\chi_0 = 10^2$ that $t_{50} \sim 7t_*$ in both T0.01L_W and T1L_W. Nevertheless, we find that the lifetime of the cloud is still significantly longer than that in a hot wind.

In order to compare cloud in radiation and in hot wind,

we perform three hydrodynamic simulations H1, H2 and H3 with Mach number of the hot wind $M_{\text{hot}} = 5, 10, 20$ (see Section 2.6 and Table 1). We translate code units back to cgs units for comparisons. The evolution of cloud mass in hot winds $M_c/M_{c,i}$ is shown in Figure 17. Compared to T1L and T1L_W runs, we find that cloud mass drops significantly faster in hot winds. According to our simulations, the cloud survival time $t_{50} \sim 8.6 \times 10^3$ yr for H1 ($M_{\text{hot}} = 5$), $t_{50} \sim 1.8 \times 10^4$ yr for H2 ($M_{\text{hot}} = 10$), and $t_{50} \sim 3.6 \times 10^4$ yr for H3 ($M_{\text{hot}} = 20$) respectively. The values of t_{50} we obtained are relatively lower than those in Scannapieco & Brüggén (2015) (see also Schneider & Robertson 2017), who gives $t_{50} = \alpha\sqrt{1 + M_{\text{hot}}t_{cc}}$ with the crushing time if the cloud in a hot flow $t_{cc} = \chi_0^{1/2}(R_c/V_{\text{hot}})$. Scannapieco & Brüggén (2015) found that $\alpha \approx 4$, but we find lower efficiency that $\alpha \approx 1.3, 0.9$ and 0.7 in H1, H2 and H3 respectively. The differences can be caused by the adiabatic background and the parameter sets we used in the paper. We choose the initial cloud density $\rho_* \sim 10^{-20}$ g cm $^{-3}$, which is four orders of magnitude higher than the cloud density in Scannapieco & Brüggén (2015); and we use $T_{\text{hot}} = 10^6$ K and $T_c = 10^2$ K, which are lower than the values in Scannapieco & Brüggén (2015). However, even we adopt t_{50} in Scannapieco & Brüggén (2015) for our parameter set, we have

$$t_{50}^{\text{SB}} \simeq 2.4 \times 10^3 \text{ yr} (\alpha/4) M_{\text{hot}}^{3/2} \tau_*, \quad (30)$$

thus in H1, H2 and H3 the clouds have $t_{50}^{\text{SB}} \simeq 2.6 \times 10^4$ yr, $t_{50}^{\text{SB}} \simeq 7.6 \times 10^4$ yr and $t_{50}^{\text{SB}} \simeq 2.1 \times 10^5$ yr for $M_{\text{hot}} = 5, 10$ and 20 respectively (see the dots in Figure 17), which are still significantly lower than t_{50} obtained from the cloud radiation runs $t_{50} \gg 10^6$ yr for T1L and $t_{50} \sim 7.5 \times 10^5$ yr for T1L_W. Equation (30) also shows that the cloud survival time is independent of χ_0 . We conclude that the survival time of the cloud t_{50} is much longer than t_{50} of the cloud entrained in a hot wind. The survival time of clouds in various runs are summarized in Table 2.

Cloud Survival Time Results		
Runs	t_{50} (yr)	t_{50}^{SB} (yr)
T0.01L.W	7.3×10^5	
T1L.W	7.4×10^5	
T1L	$> 10^6$	
$M_{\text{hot}} = 5$	8.6×10^3	2.6×10^4
$M_{\text{hot}} = 10$	1.8×10^4	7.6×10^4
$M_{\text{hot}} = 20$	3.6×10^4	2.1×10^5

TABLE 2

NOTE: THE CLOUD SURVIVAL TIME t_{50} IS OBTAINED FROM OUR SIMULATIONS MENTIONED IN SECTION 4.1. THE HOT WIND RUNS H1, H2 AND H3 HAVE HOT FLOW MACH NUMBER $M_{\text{hot}} = 5, 10, 20$ RESPECTIVELY, WHILE t_{50}^{SB} IS OBTAINED FROM SCANNAPIECO & BRÜGGEN (2015) (EQUATION 30 IN THIS PAPER) WITH THE SAME HOT FLOW MACH NUMBERS.

4.2. Cooling and Heating in the Background

So far we assume the background is adiabatic. Once the radiation pressure accelerates the cloud, the interface between the cloud and background is heated and becomes hotter than the background. The cooling timescale in the background and the interface region can be estimated by $t_{\text{cool}} \sim 3kT/(n_{\text{hot}}\Lambda(T))$, where n_{hot} is the density of the hot gas, and the cooling function $\Lambda(T)$ can be approximated as (Draine 2011)

$$\Lambda(T) \simeq 1.1 \times 10^{-22} T_6^{-0.7} \text{ erg cm}^3 \text{ s}^{-1} \quad (31)$$

for $10^5 \text{ K} \lesssim T \lesssim 10^{7.3} \text{ K}$, where $T_6 = T/10^6 \text{ K}$ is the gas temperature in the interface region. Thus, we estimate the cooling timescale for large-scale runs is

$$t_{\text{cool}} \sim 9.8 \times 10^4 \text{ yr } T_6^{1.7} \chi_{0.4} \tau_*^{-1}. \quad (32)$$

Compared to equation (11), we find that the condition $t_{\text{cool}} \lesssim t_*$ holds for $\chi_0 = 10^4$ with $\tau_* = 1$. The hot background with $T_{\text{bkgd}} = 10^6 \text{ K}$ can quickly cool down before the cloud is accelerated. However, heating either from supernova explosions or superwinds from massive stars, or photoheating in the rapidly star-forming environment can balance cooling in the hot background so that the background remains hot.

Here we carry out several runs to study the effects of cooling and heating in the background. T1L_cooling is based on the fiducial run T1L but includes cooling and heating in the background, other initial conditions are the same as in T1L. We compute the cooling rate from interpolating the cooling table in Schure et al (2009), who calculated the cooling rate of a hot plasma in collisional ionization equilibrium (see also Wiersma et al. 2009, Oppenheimer & Schaye 2013). The heating rate Γ is assumed to balance the initial cooling rate in the background so the un-disrupted background keeps a constant temperature $T_{\text{bkgd}} = 10^6 \text{ K}$. We find that heating and cooling in the background does not affect dust temperature in the cloud, therefore V_{mean} is nearly identical compared to that in T1L. However, the interface between the cloud and background cools down to $\simeq T_{\text{bkgd}}$ thus the pressure from the interface region is lower than in T1L, and the filamentary structure along the vertical direction expands faster compared to that in T1L. The change of cloud morphology may also change the turbulence properties. However, the left panel of Figure 16 shows that cooling does not change the evolution of $M_c/M_{c,i}$ dramatically in the hot background.

On the other hand, although CIE cooling is insignificant in the warm background with $T_{\text{bkgd}} = 10^4 \text{ K}$, it may still play important role to cool the interface between the cloud and background and to confine the shape of the clouds. We carry out two runs T0.01L.W_cooling and T1L.W_cooling which are based on T0.01L.W and T1L.W respectively, but include CIE cooling in the background. We find that the interface between the cloud and background cools down so that the clouds feel less thermal pressure from the interface, the asymptotic cloud mean velocity for T1L.W_cooling is $V_{\text{mean}} \sim 330c_{s,*}$, slightly higher than $V_{\text{mean}} \sim 200c_{s,*}$ in Figure 9. Also the cloud can obtain a longer survival time. The middle panel of Figure 16 shows that the cloud mass evolution T1L.W_cooling drops more slowly than the run without cooling. However, the longer survival time of the irradiated cloud make the conclusion in Section 4.1 even more robust. Moreover, the V_{mean} profile and $M_c/M_{c,i}$ for T0.01L.W_cooling do not change significantly compared to the run with an adiabatic background.

Also, adding cooling and heating in the hot background to maintain $T_{\text{bkgd}} = 10^6 \text{ K}$ may change the cloud evolution in hot flows. We find that t_{50} increases by a factor of several compared to the values of H1, H2 and H3 runs. However, they are still shorter than the constraint by equation (30). As a result, the survival time of the entrained clouds in hot flows are still shorter than it in a radiation field. In summary, cooling and heating in both hot and warm ionized background may slightly change the cloud morphologies, but do not change our main results qualitatively.

4.3. Cloud Turbulence and Molecular Weight

The initial structure of a cloud may affect its dynamics and lifetime. Schneider & Robertson (2017) (see also Schneider & Robertson 2015) examined that a turbulent cloud is destroyed more quickly than homogeneous cloud in the hot wind. We adopted a random density perturbation $\delta\rho/\rho$ distributed between -0.25 and 0.25 for all the simulations in Section 2.2. Here we carry out a simulation for a turbulent cloud. Using the initial and boundary conditions in T1L, in the cloud we apply an initial perturbed turbulent velocity field following a Gaussian random distribution with a Fourier power $|v^2(k)| \propto k^4$ (e.g., Ostriker et al. 2001; Gong & Ostriker 2011; Chen & Ostriker 2015). The initial velocity turbulence may cause density turbulence in the cloud, meanwhile the cloud is accelerated by radiation. The filamentary structure formed during cloud acceleration in this run is twisted due to the initial turbulence, thus the morphology of the cloud changes by cloud turbulence. On the other hand, we find that the cloud survival time $t_{50} \sim 7.7 t_*$, which is slightly shorter than it for T1L. However, the cloud t_{50} is still significantly longer than that in the hot wind. Also we find that the change of V_{mean} due to turbulence is about $\sim 4\%$ at $t = 7 t_*$. Therefore we conclude that the effects of turbulence on cloud acceleration and survival time is insignificant.

Also we assumed the molecular weight $\mu = 1$ for our simulations in Section 3. However, molecular weight may vary for different state of gas. For example, molecular weight $\mu \simeq 0.6$ for fully ionized gas with a solar-metallicity, while $\mu \simeq 2.33$ for neutral molecular gas. Here we perform another run based on T1L but with

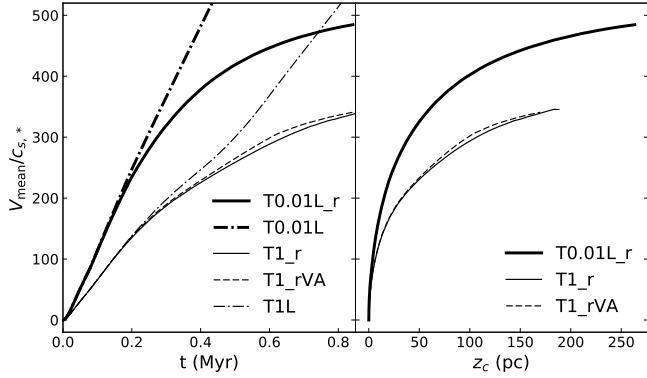


FIG. 18.— Cloud mean velocity as a function of time (left panel) and flying distance z_c (right panel) for runs T0.01L_r, T1L_r with hot background and T1L_rVA with vacuum background, where the flux is given by equation (33) and $R = 200$ pc. The velocity V_{mean} from T0.01L and T1L also plotted in the left panel.

$\mu = 2.33$ in the molecular cloud, and $\mu = 0.6$ in the fully ionized hot background, thus the background temperature has a lower value of $T_{\text{bkgd}} = (0.6/2.33)\chi_0 T_* \simeq 2.6 \times 10^5$ K. We find a slightly lower acceleration in the run with changed μ with V_{mean} decreasing to $\sim 95\%$ and $\sim 90\%$ of its values at $t = 7t_*$ and $t = 8t_*$ in T1L respectively. Also we find that the cloud mass evolution $M_c/M_{c,i}$ shows very similar behavior in this run compared to T1L, suggesting that changing μ does not change our conclusions.

4.4. Flux Variation and Vacuum Background

If the cloud flying distance z_c (see Section 2.5) is comparable to the size of the radiation-dominated region of the galaxy, the assumption of a constant flux boundary breaks down. For example, Thompson et al. (2015) studied the acceleration of dusty radiation-pressure-driven clouds with a spherical flux $F \propto r^{-2}$ semi-analytically, where clouds are assumed as spheres, and clouds expand in vacuum freely with its sound speed. Here, we perform four runs (T0.01L_r, T0.01L_rVA, T1L_r and T1L_rVA) which have the same setup as T0.01L and T1L respectively, but the boundary flux injection satisfies

$$F = F_* \frac{R^2}{(R + z_c)^2}, \quad (33)$$

where we choose the size of the starburst region as $R = 200$ pc. Also we consider two types of background medium, one is the hot background ($\chi_0 = 10^4$ for T0.01L_r and T1L_r), another is the “vacuum background” (T0.01L_rVA and T1L_rVA), in which we set $T_{\text{bkgd}} = T_*$ and a low density $\rho = 10^{-6}\rho_*$ in the background. The pressure of the cloud cannot be confined by the vacuum background so it can expand freely with its internal sound speed. Figure 18 shows the results of V_{mean} as a function of time and flying distance. We stop the simulations at $t = 8t_*$ but we use Myr and pc instead of code time and length units for Figure 18. T0.01L_r and T0.01L_rVA show almost identical acceleration history so we only plot one of them. The difference between V_{mean} from T1L_r and T1L_rVA is also negligible, which means that free expansion does not change the dynamics of cloud up to $\tau_* = 1$. The cloud velocities are significantly lower than V_{mean} from constant-flux

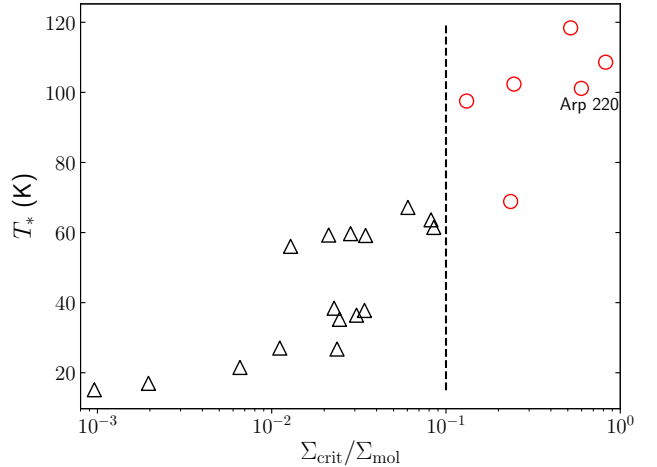


FIG. 19.— Estimated dust temperature vs. Eddington ratio $\Sigma_{\text{crit}}/\Sigma_{\text{mol}}$ using samples from Barcos-Muñoz et al. (2017). Triangles are data with $\Sigma_{\text{crit}}/\Sigma_{\text{mol}} < 0.1$ and circles are data with $\Sigma_{\text{crit}}/\Sigma_{\text{mol}} > 0.1$. Also the starburst galaxy Arp 220 is marked.

runs. Note that since F_* decreases along the vertical direction, the dust temperature also drops. We find that $T_c \sim (F_*/4)^{1/4} T_c \sim 0.85 T_*$ at $z_c = R$, thus dust in the cloud is still in thermal equilibrium with the radiation field. The decreases opacity combines with dropping flux together to affect the cloud velocity. Cloud with $\tau_* = 0.01$ can be accelerated to $z_c \simeq R = 200$ pc with $V_{\text{mean}} \sim 470 c_{s,*}$ (420 km s^{-1}) at $t \sim 0.7$ Myr, while clouds with $\tau_* = 1$ can be accelerated to $z_c \simeq R = 200$ pc at ~ 0.9 Mpc with a velocity of $V_{\text{mean}} \sim 350 c_{s,*}$ (310 km s^{-1}). Compared to Figures 1 and 3, the cloud velocity V_{mean} drops to $\sim 60\%$ of its value at the same radial position compared to the constant flux run. We also check that for a larger star-forming core $R = 500$ pc V_{mean} decreases to $\sim 75\%$ of its value for constant-flux case at $z_c = R$.

4.5. Implications to LIRGs and ULIRGs

The pancake structure of clouds along the line of sight has been observed via narrow absorption line (NAL) or broad absorption line (BAL) in AGN environments (e.g., Hall et al. 2007; Rogerson et al. 2011; Hamann et al. 2013). Proga et al. (2014) performed radiation hydrodynamics to model the pancake structure of the irradiated clouds in AGNs. Analogously, we suggest that future observations of cloud morphologies may give a hint on the mechanism of cloud acceleration in LIRGs and ULIRGs. Optically thin clouds with column density $N_{\text{H}} \sim 10^{21} \text{ cm}^{-2}$ has the typical columns observed in galactic winds (Martin 2005; Martin et al. 2015). We find that these clouds develop pancake structure due to radiation pressure on dust, while the entrained clouds in hot flows fragment into small pieces and stretch out along the direction of motion. The different theoretical predictions of cloud evolution can be potentially used to guide future observations.

The gravity contributed by galactic disk, bulge and halo can further decreases V_{mean} . Dust in a cloud can be considered to be in thermal equilibrium with the radiation field, therefore the infrared flux from the galactic disk can be calculated by equation (9). The critical disk density can be given by $2\pi G \Sigma_{\text{crit}} = g_*$, where g_* is from

equation (10). Combining equations (9) and (10) we obtain

$$\Sigma_{\text{crit}} = 2.7 \times 10^4 T_{*,2}^6 M_{\odot} \text{ pc}^{-2}. \quad (34)$$

If the galactic surface density $\Sigma > \Sigma_{\text{crit}}$, the LIRG/ULIRG system is a sub-Eddington system. Note that the opacity we used (equation 8) assumes a Milky-Way-like dust-to-gas ratio. The actually Σ_{crit} is proportional to the dust-to-gas ratio, which is still uncertain in most galaxies.

We have used a fiducial dust temperature $T_* = 100$ K in all simulations. In fact, the cloud temperature can be estimated from the observed flux, assuming thermal equilibrium between radiation and dust in the atmosphere of the galaxy. Taking data from Barcos-Muñoz et al. (2017) (Table 6) as samples, we estimate that the temperature of dusty clouds has a range of $T_c \sim 15 - 120$ K. Also we can calculate Σ_{crit} using equation (34), and compared with molecular surface density Σ_{mol} which gives the lower bound of galactic surface density Σ . As mentioned in Zhang & Davis (2017), we find all the samples in Barcos-Muñoz et al. (2017) give $\Sigma_{\text{crit}} < \Sigma_{\text{mol}}$, thus all of them are sub-Eddington systems. However, Thompson & Krumholz (2016) showed that a fraction of gas in the star-forming core can still be locally super-Eddington even for a sub-Eddington system. The mass probability distribution for $\Sigma_{\text{crit}}/\Sigma > 0.1$ is $\sim 10^{-3} - 2 \times 10^{-2}$, while the area probability distribution for $\Sigma_{\text{crit}}/\Sigma > 0.1$ is $\sim 0.04 - 0.4$, depending on the property of gas turbulence. This scenario can explain the origin of cloud launching by radiation pressure from a sub-Eddington system. Figure 19 shows the estimated T_* vs. global Eddington ratio $\Sigma_{\text{crit}}/\Sigma_{\text{mol}}$ for the samples in Barcos-Muñoz et al. (2017). Interestingly, we find that the dust temperature correlates with the Eddington ratio $\Sigma_{\text{crit}}/\Sigma_{\text{mol}}$, and most galaxies with $\Sigma_{\text{crit}}/\Sigma_{\text{mol}} > 1$ have $T_* \sim 100 - 120$ K. For example, we estimate that Arp 220 has $\Sigma_{\text{crit}}/\Sigma_{\text{mol}} \sim 0.6$ with $T_c \sim 100$ K, a value between the warm dust temperature in eastern and western nuclei (e.g., Wilson et al. 2014; Scoville et al. 2015). We estimate the upper bound velocity for a 10-pc size cloud with a decreasing factor ϵ compared to the case of constant flux with gravity can reach

$$V_c \sim 310 \text{ km s}^{-1} \left(\frac{\epsilon}{0.6} \right) \left(\frac{t}{0.7 \text{ Myr}} \right) \times \left(\frac{F_*}{5.6 \times 10^{13} L_{\odot} \text{ kpc}^{-2}} \right)^{3/2}, \quad (35)$$

which may explain the observations of molecular outflows in LIRGs and ULIRGs (Sakamoto et al. 1999; Walter et al. 2002; Veilleux et al. 2005 and references therein; Veilleux et al. 2009; Fischer et al. 2010; Bolatto et al. 2013; Ciccone et al. 2014; Walter et al. 2017).

5. CONCLUSIONS

We study cold clouds accelerated by ram pressure on dust in the environment of rapidly star-forming galaxies dominated by infrared radiation flux. We perform a series of 2D and 3D radiation hydrodynamic simulations, utilizing the reduced speed of light approximation to solve the frequency-averaged, time-dependent radiative transfer equation. The radiative acceleration of a

cloud in pressure equilibrium with a surrounding hot, tenuous medium can be described by

$$V_{\text{mean}} = \epsilon \frac{\kappa_R F_*}{c}, \quad (36)$$

where κ_R is the Rosseland mean opacity for the dust, F_* is the radiation flux (equations 23 and 25). The coefficient ϵ mainly depends on the initial optical depth of the cloud. We obtain $\epsilon \sim 1.4$ for very optically thin clouds, and ϵ decreases from $\epsilon \sim 0.8$ to $\epsilon \sim 0.18$ for optically thick clouds from $\tau_* = 1$ to $\tau_* = 10$. Empirically we have $\epsilon \simeq \min\{1, \exp(1.3 - 1.5\tau_*^{0.3})\}$ to fit cloud acceleration from optically thin to thick clouds up to $\tau_* \sim 10$ (equation 27). However, the gas pressure in the interface between the background and the front of the cloud may decelerate and destroy the irradiated cloud if the cloud is embedded in a warm medium $T_{\text{bkgd}} \lesssim 10^4$ K that the initial density ratio between the cloud and background $\chi_0 = \rho_*/\rho_{\text{bkgd}} \lesssim 10^2$ (Figure 9).

The evolution of the cloud geometry and morphology during its acceleration depends on its characteristic lengthscale and other attributes. In general, an optically thin cloud with a size of ~ 10 pc is squeezed in the direction of motion to form a pancake structure (Figure 1), which is caused by the combination of radiation pressure, gas pressure from the interface between the front of the cloud and the background, as well as ram pressure of the background. On the other hand, differential acceleration of an optically thick, ~ 10 pc cloud forms a filamentary shape elongated parallel to the acceleration direction extending to ~ 100 pc (Figure 3). A much smaller cloud with the same initial column density/optical depth and same χ_0 , but smaller characteristic lengthscale may also form a pancake or filamentary structure, but eventually fragments into small pieces due to shearing instabilities between the cloud and background (Figure 7). The morphology of cloud is somewhat sensitive to various assumptions: different reduction factors of the reduced speed of light, spatial resolution, cooling and heating processes in the background, initial turbulence profile, and perturbation inside the cloud, as well as the dimensionality of the simulation. However, the dynamics of cloud acceleration is only weakly affected by these assumptions, unless a dense background $\chi_0 \lesssim 10^2$ is present to shred the cloud.

We also compare the dynamics of the cloud accelerated by radiation fields to an entrained cloud in a hot flow driven by supernovae in the host galaxy in a limit where the momentum injection of the hot flow is the same as the momentum of radiation. The cloud survival time is defined as half of the initial cloud mass is still above 1/3 of its initial average density. Although the survival time of clouds in hot flows is shorter in our hydrodynamic simulations compared to the literature, and the cloud is shredded much faster in a warm medium compared to a hot medium, we find the the survival time is still significantly longer for irradiated cloud than the hot-flow-entrained cloud even including all the uncertainties (Figures 16 and 17). Therefore, a cloud in a radiation-dominated region can be accelerated to a higher velocity with a larger distance compared to a cloud in the hot flow environment. This result can be apply to LIRGs and ULIRGs, and we find that dusty clouds in LIRGs and ULIRGs can be accelerated to hundreds of km s^{-1}

and potentially match the observations.

We thank Todd Thompson, Daniel Proga, Peng Oh, Mike McCourt, Sylvain Veilleux, Eliot Quataert, Norm Murray, Tim Waters, Suoqing Ji, Patrick Hall, Ari Laor and Sebastian Hoenig for stimulating discussions. This work used the computational resources provided by the Advanced Research Computing Services (ARCS) at the University of Virginia. We also used the Ex-

treme Science and Engineering Discovery Environment (XSEDE), which is supported by National Science Foundation (NSF) grant No. ACI-1053575. S. W. D. and D. Z. acknowledge support from NSF grant AST-1616171 and an Alfred P. Sloan Research Fellowship. Y. F. J is supported part by the National Science Foundation under Grant No. NSF PHY 17-48958. J. M. S. is supported by NSF grant AST-1333091.

APPENDIX

A. REDUCED SPEED OF LIGHT APPROXIMATION

The dimensionless radiation hydrodynamics equations include two ratios $\mathbb{C} = c/a_*$ (see the definition in Section 2.4) and $\mathbb{P} = a_* T_*^4 / P_*$, where a_* , T_* and P_* are the characteristic velocity, temperature and pressure respectively (Jiang et al. 2012). The dimensionless time-step Δt in the explicit algorithm is constrained by the Courant condition

$$\Delta t < C_{\text{CFL}} \frac{\Delta z}{\mathbb{C}}, \quad (\text{A1})$$

where the dimensionless Δz is the cell width in the computational box (see Table 1). In the paper we fix the Courant–Friedrichs–Lewy number to be $C_{\text{CFL}} = 0.4$ for 2D runs expect for T1LR3_{lowCFL}, and $C_{\text{CFL}} = 0.3$ for 3D runs (see also Jiang et al. 2014). Therefore, for cloud $T_* = 100$ K and $a_0 = c_{s,*}$, we have $\mathbb{C} \simeq 3.3 \times 10^5$, and the Courant condition equation (A1) gives a severe constraint on Δt that $\Delta t < 8 \times 10^{-7} \Delta z$. In order to reduced the computational costs, we use the reduced speed of light approximation, which has been implemented in radiation hydrodynamical simulations (Gnedin & Abel 2001; González et al. 2007; Aubert & Teyssier 2008; Petkova & Springel 2011; Rosdahl et al 2013; Skinner & Ostriker 2013, 2015; Gnedin 2016). The parameter $\tilde{\mathbb{C}}$ is used instead of \mathbb{C} before the radiation source terms (see equations 17 in Section 2.4).

The domain of validity for the reduced speed of light approximation is well described in Section 3.2 of Skinner & Ostriker (2013) along with references therein. The main logic of the approximation is that signal propagation on the light crossing time is often irrelevant in systems where the radiation transfer is dominated by local interactions between the radiation field and matter. The key constraint in these systems is then on maintaining the correct ordering of dynamic timescale $t_{\text{dyn}} \sim L/v_{\text{max}}$ and the diffusion timescale $t_{\text{diff}} \sim L\tau_{\text{max}}/c$, where L is the characteristic size of the system. To maintain the correct ordering, the lower bound of $\tilde{\mathbb{C}}$ is constrained by

$$\tilde{\mathbb{C}} \gg \frac{v_{\text{max}}}{a_*} \max\{1, \tau_{\text{max}}\}. \quad (\text{A2})$$

The main difficulty with enforcing this criterion is determining the appropriate values for v_{max} and τ_{max} , which are nominally the maximum velocity and optical depth in the system, respectively. In practice, τ_{max} requires a choice of a characteristic length over which to define the optical depth. A conservative approach would take the the maximum optical depth anywhere in the system. However, this may still result in a timestep that is unnecessarily small if the largest velocities occur only in optically thin regions. Therefore, the choice for the reduction factor requires careful consideration and testing.

In order to justify the reduced speed of light approximation and confirm the validity of the above criterion, we use the radiation ATHENA++ code to do several test simulations. We first consider the impact on radiative linear waves, where we can analytically compute the dispersion relation in the reduced speed of light approximation and then consider the more complex case of dusty gas accelerated by radiation pressure.

A.1. Linear Wave Test

We test the 1D linear wave in radiation hydrodynamics. The dispersion relation between ω and k is given by Johnson & Klein (2010) (see also Jiang et al. 2012), where ω and k are the angular frequency and the wavenumber respectively. We generalize these derivations in a straightforward manner to include the reduction factor \mathbb{R} . The background is setup to be $\rho = P = T = 1$, the ratios \mathbb{P} and \mathbb{C} were varied, but for brevity we only show the case with $\mathbb{P} = 1$ and $\mathbb{C} = 1000$. We choose the reduction factor $\mathbb{R} = 1, 0.1$ and 0.01 , which gives $\tilde{\mathbb{C}} = 1000, 100$ and 10 respectively. Figure 20 shows the effects of reduced speed of light depending on the optical depth per wavelength in the linear wave system. Since ω can be a complex number, the ratio of its real part and k that ω_{R}/k defines the wave propagation speed, and the imaginary part ω_{I} defines the wave damping rate. Note that the curves in Figure 20 are given by analytic results, and the circles represent the values of ω_{R} and ω_{I} that are obtained by fitting the ATHENA++ results after running for one adiabatic wave period. We see the effects of the reduced speed of light approximation in both the phase velocity and the damping rate, with the most significant effect in the damping rates. The damping rate should turn over at $\tau \sim 10^3$ with $\mathbb{C} = 1000$, but it turns over at lower optical depth at $\tau \sim \tilde{\mathbb{C}}$ for reduced speed of light cases. We considered other values of \mathbb{C} (not shown) and confirm that this results holds quite generally. Hence, the reduced speed of light approximation is valid for $\tilde{\mathbb{C}} < \tau$. Since $v_{\text{max}} \simeq a_*$, this result is consistent with equation (A2). We find

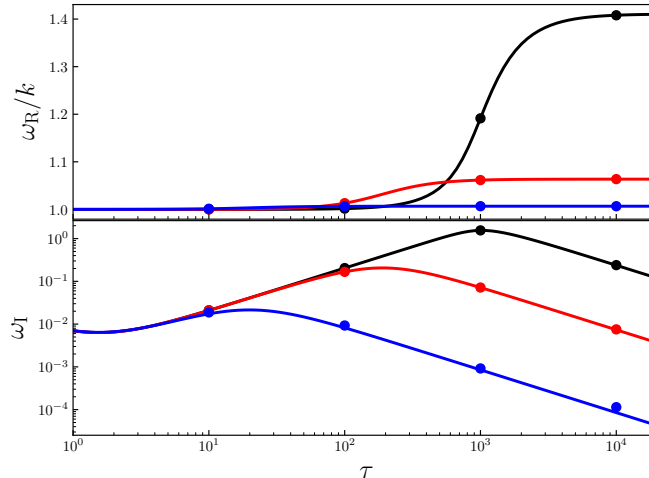


FIG. 20.— Comparison of the wave propagation speed (upper panel) and the damping rate of linear waves (lower panel) as function of optical depth per wavelength, where $\mathbb{P} = 1$, $\mathbb{C} = 1000$, and the reduction factor $\mathbb{R} = 1$ (black lines), 0.1 (red lines) and 0.01 (blue lines). The curves are the analytical solutions, and the circles are simulation results given by ATHENA++. Note that our resolution study implies that the slight mismatch between the simulation and analytic curve for $\mathbb{R} = 0.01$ at $\tau = 10^4$ is due to the limits of resolution giving rise to numerical diffusion and does not imply a problem with our implementation of the reduced speed of light approximation.

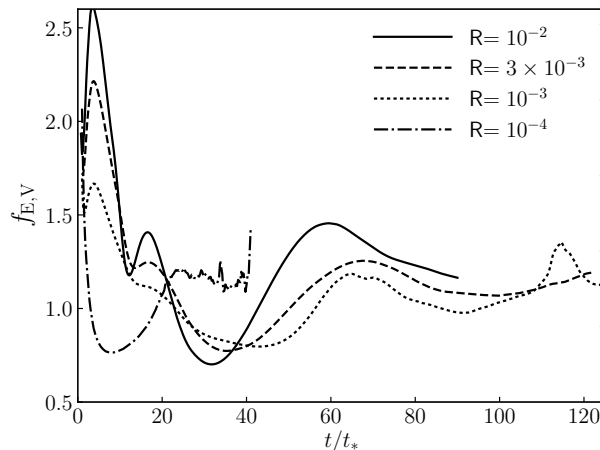


FIG. 21.— Volume-weighted Eddington ratio $f_{E,V}$ as a function of time for four runs $\mathbb{R} = 10^{-2}, 10^{-3}, 3 \times 10^{-3}$ and 10^{-4} . The initial and boundary conditions are the same as in the T3_F0.5 run in Davis et al. (2014).

that the ATHENA++ results agree quite well with the curves, and confirm convergence in the L1 norm as resolution increases. These results would tend to confirm that the reduced speed of light approximation is implemented correctly in the ATHENA++ radiation module.

A.2. Radiation-Pressure-Driven Galactic Winds

Radiation pressure on dust can drive large-scale galactic winds (Murray et al. 2005). In particular, the problem of the two-dimensional radiation hydrodynamic of a column of gas that is accelerated by a constant infrared radiation flux has been studied first by Krumholz & Thompson (2012, 2013), then by others using a variety of algorithms (Davis et al. 2014; Tsang & Milosavljević 2015; Rosdahl & Teyssier 2015; Zhang & Davis 2017). Here we redo this problem using the radiation ATHENA++ code. The initial and boundary conditions are the same as the T3_F0.5 run in Davis et al. (2014): we assume the initial infrared optical depth of the dusty gas is $\tau_* = 3$, the gas temperature is $T_* = 82$ K, the infrared flux $F_* = a_r c T_*^4$, the dusty opacity κ_R follows equation (8) in this paper, and the initial dimensionless Eddington ratio is setup as $f_{E,*} = \kappa_R F_*/(gc)$, where g is the gravity. The scale height is $h_* = c_{s,*}^2/g$, and the size of the box is $[L_x \times L_y]/h_* = 500 \times 3200$ with a resolution of $\Delta x/h_* = 1$. We choose the reduced speed of light $\mathbb{R} = 10^{-2}, 3 \times 10^{-3}, 10^{-3}$ and 10^{-4} , and carry out four runs. The runs stop once the gas hits the top of the box except for the run with $\mathbb{R} = 10^{-4}$. We find that the gas eventually becomes unbound. This result is similar as that in

Davis et al. (2014). An important parameter to measure the properties of a unbound gas is the Eddington ratio

$$f_{E,V} = \frac{\langle \kappa_R \rho F \rangle}{cg \langle \rho \rangle}. \quad (\text{A3})$$

Figure 21 shows $f_{E,V}$ as a function of time. We find although there are initial bumps at early time, the Eddington ratio $f_{E,V}$ converges to $f_{E,V} \sim 1$ for $\mathbb{R} \geq 10^{-3}$ at later time. The reduced speed of light approximation breaks down at $\mathbb{R} = 10^{-4}$. We stops $\mathbb{R} = 10^{-4}$ run at $t \simeq 40 t_*$, otherwise the solution becomes unstable. We use the vertically integrated optical depth to estimate τ_{\max} and find that $\tau_{\max} \sim 20$. Also, we get $v_{\max}/c_{s,*} \sim 20$, thus the criterion equation (A2) gives $\tilde{C} \gg 400$, or $\mathbb{R} \gg 7 \times 10^{-4}$. This result is consistent with Figure 21.

REFERENCES

- Andrews, B. H., & Thompson, T. A. 2011, *ApJ*, 727, 97
Aguirre, A., et al. 2001a, *ApJ*, 556, 11
Aguirre, A., et al. 2001b, *ApJ*, 561, 521
Aubert, D., & Teyssier, R. 2008, *MNRAS*, 387, 295
Barai, P., et al. 2013, *MNRAS*, 430, 3213
Barcos-Muñoz, L., Leroy, A. K., Evans, A. S., Condon, J., & Privon, G. C., et al. 2017, *ApJ*, 843, 117
Barkana, R., & Loeb, A. 1999, *ApJ*, 523, 54
Benson, A. J., et al. 2003, *ApJ*, 599, 38
Bisbas, T. G., Haworth, T. J., Barlow, M. J., Viti, S., Harries, T. J., Bell, T., & Yates, J. A. 2015, *MNRAS*, 454, 2828
Bolatto, Alberto D., Warren, Steven R., Leroy, Adam K., et al. 2013, *Nature*, 499, 450
Bower, R. G., Benson, A. J., & Crain, R. A. 2012, *MNRAS*, 422, 2816
Brüggen, M., & Scannapieco, E.
Chen, C.-Y., & Ostriker, E. C. 2015, *ApJ*, 810, 126
Chevalier, R. A., & Clegg, A. W. 1985, *Nature*, 317, 44
Chisholm, J., Tremonti, C. A., Leitherer, C., & Chen, Y. 2017, *MNRAS*, in press
Cicone, C. et al. 2014, *A&A*, 562, 21
Cooper, J. L., Bicknell, G. V., Sutherland, R. S., & Bland-Hawthorn, J. 2008, *ApJ*, 674, 157
Cooper, J. L., Bicknell, G. V., Sutherland, R. S., & Bland-Hawthorn, J. 2009, *ApJ*, 703, 330
Cowie L. L., & McKee C. F. 1977, *ApJ*, 211, 135
Davis, S. W., Stone, J. M., & Jiang, Y.-F. 2012, *ApJS*, 199, 9
Davis, S. W., Jiang, Y.-F., Stone, J. M., & Murray, Norman 2014, *ApJ*, 796, 107
Dekel, A., & Silk, J. 1986, *ApJ*, 303, 39
Draine, B. T. 2003, *ApJ*, 598, 1017
Draine, B. T. 2011, *Physics of the Interstellar and Intergalactic Medium* by Bruce T. Draine. Princeton University Press, 2011, ISBN: 978-0-691-12214-4
Erb, D. K. 2008, *ApJ*, 674, 151
Faucher-Giguère, C., Quataert, E., & Murray, N. 2012, *MNRAS*, 420, 1347
Finlator, K., & Davé, R. 2008, *MNRAS*, 385, 2181
Finlator, K., Özel, F., & Davé, R. 2009, *MNRAS*, 393, 1090
Fischer, J., Sturm, E., González-Alfonso, E. et al. 2010, *A&A*, 518, 41
Fujita, A., Martin, C. L., Mac Low, M.-M., et al. 2009, *ApJ*, 698, 693
Gnedin, N. Y. 2016, *ApJ*, 833, 66
Gnedin, N. Y., & Abel, T. 2001, *NewA*, 6, 437
Goldsmith P. F., 2001, *ApJ*, 557, 736
Gong, H., & Ostriker, E. C. 2011, *ApJ*, 729, 120
González-Alfonso, E., Smith, H. A., Fischer, J., & Cernicharo, J. González, M., Audit, E., & Huynh, P. 2007, *A&A*, 464, 429
Hamann, F., Chartas, G., McGraw, S., Rodriguez Hidalgo, P., Shields, J., Capellupo, D., Charlton, J., & Eracleous, M. 2013, *MNRAS*, 435, 133
Hall, P. B., Sadavoy, S. I., Hutsemekers, D., Everett, J. E., & Rafiee, A. 2007, *ApJ*, 665, 174
Heckman, T., Lehnert, M. D., Strickland D. K., & Lee, A. 2000, *ApJS*, 129, 493
Heckman, T. M., & Thompson, T. A. 2017, arXiv:1701.09062
Hopkins, P. F., Quataert, E., & Murray, N. 2012, *MNRAS*, 421, 3522
Iliev, I. T., Moore, B., Gottlöber, S., Yepes, G., Hoffman, Y. & Mellema, G. 2011, *MNRAS*, 413, 2093
Ipavich, F. M. 1975, *ApJ*, 196, 107
Jiang, Y.-F., Guillochon, J., & Loeb, A. 2016, *ApJ*, 830, 125
Jiang, Y.-F., Stone, J. M., & Davis, S. W. 2012, *ApJS*, 199, 14
Jiang, Y.-F., Stone, J. M., & Davis, S. W. 2014, *ApJS*, 213, 7
Jiang, Y.-F., Stone, J. M., & Davis, S. W. 2017, arXiv: 1709.02845
Johnson, B. M., & Klein, R. I. 2010, *J. Quant. Spectrosc. Radiat. Transfer*, 111, 723
Klein, R. I., McKee, C. F., & Colella, P. 1994, *ApJ*, 420, 213
Kennicutt, R.C. 1998, *ARA&A*, 36, 189
Kornei, K. A., et al. 2013, *ApJ*, 774, 50
Krumholz, M. R., Klein, R. I., McKee, C. F., & Bolstad, J. 2007, *ApJ*, 667, 626
Krumholz, M. R., & Thompson, T. A. 2012, *ApJ*, 760, 155
Krumholz, M. R., & Thompson, T. A. 2013, *MNRAS*, 434, 2329
Larsen, E. W., & Wollaber, A. B. 2008, *NSE*, 160, 267
Larsen, R. B. 1974, *MNRAS*, 169, 229
Levermore, C. D., & Pomraning, G. C. 1981, *ApJ*, 248, 321
Makiya, R., Totani, T., Kobayashi, M. A. R., Nagashima, M., & Takeuchi, T. T. 2014, *MNRAS*, 441, 63
Martin, C. L. 1998, *ApJ*, 506, 222
Martin, C. L. 2005, *ApJ*, 621, 227
Martin, C. L., Dijkstra, M., Henry, A., Soto, K. T., Danforth, C. W., & Wong, J. 2015, *ApJ*, 803, 6
McCourt, M., Oh, S. Peng, O’Leary, R. M., & Madigan, A.-M. 2016, arXiv: 1610.01164
McCourt, M., O’Leary, R. M., Madigan, A.-M., & Quataert, E. 2015, *MNRAS*, 449, 2
McKinney, J. C., Tchekhovskoy, A., Sadowski, A., & Narayan, R. 2014, *MNRAS*, 441, 3177
Murray, N., Martin, C. L., Quataert, E., & Thompson, T. A. 2007, *ApJ*, 660, 211
Murray, N., Ménard, B., & Thompson, T. A. 2011, *ApJ*, 735, 66
Murray, N., Quataert, E., & Thompson, T. A. 2005, *ApJ*, 618, 569
Murray, N., Quataert, E., & Thompson, T. A. 2010, *ApJ*, 709, 191
Namekata, D., Umemura, M., & Hasegawa, K. 2014, *MNRAS*, 443, 2018
Oppenheimer, B. D., et al. 2010, *MNRAS*, 406, 2325
Oppenheimer, B. D., & Schaye, J. 2013, *MNRAS*, 434, 1043
Ostriker, E. C., Stone, J. M., & Gammie, C. F. 2001, *ApJ*, 546, 980
Poludnenko, A. Y., Frank, A., & Blackman, E. G. 2002, *ApJ*, 576, 832
Peeples, M. S., & Shankar, F. 2011, *MNRAS*, 417, 2962
Petkova, M., & Springel, V. 2011, *MNRAS*, 415, 3731
Puchwein, E., & Springel, V. 2013, *MNRAS*, 428, 2966
Proga, D., Jiang, Y.-F., Davis, S. W., Stone, J. M., & Smith, D. 2014, *ApJ*, 780, 51
Proga, D., Stone, J. M., & Drew, J. E. 1998, *MNRAS*, 295, 595
Proga, D., & Waters, T. 2015, *ApJ*, 804, 137
Rogerson, J. A., Hall, P. B., Snedden, S. A., Brotherton, M. S., & Anderson, S. F.
Rosdahl, J., Blaizot, J., Aubert, D., Stranex, T., & Teyssier, R. 2013, *MNRAS*, 436, 2188
Rosdahl, J., & Teyssier, R. 2015, *MNRAS*, 449, 4380
Roth, N., & Kasen, D. 2015, *ApJS*, 217, 9
Rupke, D. S., Veilleux, S., & Sanders, D. B. 2002, *ApJ*, 570, 588
Rupke, D. S., Veilleux, S., & Sanders, D. B. 2005, *ApJS*, 160, 87
Rupke, D. S., Veilleux, S., & Sanders, D. B. 2005, *ApJS*, 160, 115
Rupke, D. S., Veilleux, S., & Sanders, D. B. 2005, *AJ*, 632, 751
Sakamoto, K., Okumura, S. K., Ishizuki, S., & Scoville, N. Z. 1999, *ApJ*, 525, 691
Scannapieco, E. 2017, *ApJ*, 837, 28

- Scannapieco, E., & Brügggen, M. 2015, *ApJ*, 805, 158
- Schartmann, M., Krause, M., & Burkert, A. 2011, *MNRAS*, 415, 741
- Schneider, E. E., & Robertson, B. E. 2015, *ApJS*, 217, 24
- Schneider, E. E., & Robertson, B. E., 2017, *ApJ*, 834, 144
- Schure, K. M., Kosenko, D., Kaastra, J. S., Keppens, R., & Vink, J. 2009, *A&A*, 508, 751
- Scoville, N. Z. 2013, in *Secular Evolution of Galaxies*, eds. J. Falcón-Barroso, & Knapen J. H., 491
- Scoville, N., Sheth, K., Walter, F. et al. 2015, *ApJ*, 800, 70
- Sekora, M. D., & Stone, J. M. 2010, *Journal of Computational Physics*, 229, 6819
- Semenov, D., Henning, T., Helling, C., Ilgner, M., & Sedlmayr, E. 2003, *A&A*, 410, 611
- Shoppell, P. L., & Bland-Hawthorn, J. 1998, *ApJ*, 493, 129
- Shapiro, P. R., Iliev, I. T., & Raga, A. C. 2004, *MNRAS*, 348, 753
- Skinner, M. A., & Ostriker, E. C. 2013, *ApJS*, 206, 21
- Skinner, M. A., & Ostriker, E. C. 2015, *ApJ*, 809, 187
- Socrates, A., Davis, S. W., & Ramirez-Ruiz, E. 2008, *ApJ*, 687, 202
- Spitzer, L. 1968, *Diffuse Matter in Space* (New York: Interscience)
- Stone, J. M., Gardiner, T. A., Teuben, P., Hawley, J. F., & Simon, J. B. 2008, *ApJS*, 178, 137
- Stone, J. M., Mihalas, D., & Norman, M. L. 1992, *ApJS*, 80, 819
- Strickland, D. K., & Heckman, T. M. 2007, *ApJ*, 658, 258
- Strickland, D. K., & Heckman, T. M. 2009, *ApJ*, 697, 2030
- Strickland, D. K., & Stevens, I. R. 2000, *MNRAS*, 314, 511
- Thompson, T. A., Fabian, A. C., Quataert, E., & Murray, N. 2015, *MNRAS*, 449, 147
- Thompson, T. A., & Krumholz, M. R. 2016, *MNRAS*, 455, 334
- Thompson, T. A., Quataert, E., & Murray, N. 2005, *ApJ*, 630, 167
- Thompson, T. A., Quataert, E., Zhang, D., & Weinberg, D. H. 2016, *MNRAS*, 455, 1830
- Tremonti, C. A., et al. 2004, *ApJ*, 613, 898
- Tsang, Benny T.-H., & Milosavljević, M. 2015, *MNRAS*, 453, 1108
- Turner, N. J., & Stone, J. M. 2001, *ApJS*, 135, 95
- Uhlig, M., Pfrommer, C., Sharma, M., Nath, B. B., Enßlin, T. A., & Springel, V. 2012, *MNRAS*, 423, 2374
- Veilleux, S., Cecil, G., & Bland-Hawthorn, J. 2005, *ARA&A*, 43, 769
- Veilleux, S., Rupke, D. S. N., & Swaters, R. 2009, *ApJ*, 700, 149L
- Vollmer, B., Gratier, P., Braine, J., & Bot, C. 2017, *A&A*, 602, 51
- Walter, F., Weiss, A., & Scoville, N. 2002, *ApJ*, 580, 21L
- Walter, F., Bolatto, A. D., Leroy, A. K. et al. 2017, *ApJ*, 835, 265
- Waters, T., & Proga, D. 2016, *MNRAS*, 460, 79
- Waters, T., Proga, D., Dannen, R., & Kallman, T. R. 2017, *MNRAS*, 467, 3160
- White, C. J., Stone, J. M., & Gammie, C. F. 2016, *ApJS*, 225, 22
- Whitney, B. A. 2011, *Bulletin of the Astronomical Society of India*, 39, 101
- Wiersma, R. P. C., Schaye, J., & Smith, B. D. 2009, *MNRAS*, 393, 99
- Wilson, C. D., Rangwala, N., Glenn, J., Maloney, P. R., Spinoglio, L., & Pereira-Santaella, M. 2014, *ApJ*, 789, 36
- Wofford, A., Leitherer, C., & Salzer, J. 2013, *ApJ*, 765, 118
- Zhang, D., & Davis, S. W. 2017, *ApJ*, 839, 54
- Zhang, D., Thompson, T. A., Murray, N., & Quataert, E. 2014, *ApJ*, 784, 93
- Zhang, D., Thompson, T. A., Murray, N., & Quataert, E. 2017, *MNRAS*, 468, 4801
- Zhang, W., Howell, L., Almgren, A., Burrows, A., & Bell, J. 2011, *ApJS*, 196, 20